

# The spin and shape of dark matter haloes in the Millennium simulation of a $\Lambda$ CDM universe

Philip Bett<sup>1,3</sup>, Vincent Eke<sup>1</sup>, Carlos S. Frenk<sup>1</sup>, Adrian Jenkins<sup>1</sup>, John Helly<sup>1</sup>,  
and Julio Navarro<sup>2</sup>

<sup>1</sup>*Institute for Computational Cosmology, University of Durham, South Road, Durham, DH1 3LE, UK*

<sup>2</sup>*Department of Physics and Astronomy, University of Victoria, Victoria, BC, V8P 5C2, Canada*

<sup>3</sup>*P.E.Bett@durham.ac.uk*

22 August 2018

## ABSTRACT

We investigate the spins and shapes of over a million dark matter haloes identified at  $z = 0$  in the Millennium simulation. Our sample spans halo masses ranging from dwarf galaxies to rich galaxy clusters. The very large dynamic range of this  $\Lambda$ CDM cosmological simulation enables the distribution of spins and shapes and their variation with halo mass and environment to be characterised with unprecedented precision. We compare results for haloes identified using three different algorithms, and investigate (and remove) biases in the estimate of angular momentum introduced by both the algorithm itself and by numerical effects. We introduce a novel halo definition called the TREE halo, based on the branches of the halo merger trees, which is more appropriate for comparison with real astronomical objects than the traditional “friends-of-friends” and “spherical overdensity” algorithms. We find that for this many objects, the traditional lognormal function is no longer an adequate description of the distribution,  $P(\lambda)$ , of the dimensionless spin parameter  $\lambda$ , and we provide a different function that gives a better fit for TREE and spherical overdensity haloes. The variation of spin with halo mass is weak but detectable, although the trend depends strongly on the halo definition used. For the entire population of haloes, we find median values of  $\lambda_{\text{med}} = 0.0367\text{--}0.0429$ , depending on the definition of a halo. The haloes exhibit a range of shapes, with a preference for prolateness over oblateness. More massive haloes tend to be less spherical and more prolate. We find that the more spherical haloes have less coherent rotation in the median, and those closest to spherical have a spin independent of mass ( $\lambda_{\text{med}} \approx 0.033$ ). The most massive have a spin independent of shape ( $\lambda_{\text{med}} \approx 0.032$ ). The majority of haloes have their angular momentum vector aligned with their minor axis and perpendicular to their major axis. We find a general trend for higher spin haloes to be more clustered, with a stronger effect for more massive haloes. For galaxy cluster haloes, this can be larger than a factor of  $\sim 2$ .

**Key words:** cosmology: dark matter – galaxies: haloes – methods:  $N$ -body simulations

## 1 INTRODUCTION

The formation of galaxies is intimately linked to the acquisition and distribution of angular momentum. In the current cosmological paradigm, the inflationary  $\Lambda$ CDM model, cosmic structures grow hierarchically. Dark matter haloes form by the dissipationless gravitational collapse of material associated with peaks in the primordial density fluctuation field, growing, through mergers and smooth accretion, into objects with a wide range of masses at the present day. Galaxies form when baryons cool and condense near the centre of these haloes (White & Rees 1978, White & Frenk

1991). They undergo mergers and tidal interactions along with their haloes, giving rise to the rich spectrum of galaxy types and environments that we see today.

Understanding the generation and evolution of the angular momentum of dark matter haloes is a prerequisite for understanding the angular momentum and morphology of galaxies. For example, the distribution of halo spins is a basic input to models of galaxy formation (e.g. Mo et al. 1998, van den Bosch 1998, Cole et al. 2000). The early evolution of the angular momentum of a density perturbation is adequately described by the linear tidal torque theory (see e.g. Hoyle 1949, Peebles 1969, Doroshkevich 1970, White

1984, Catelan & Theuns 1996, Lee & Pen 2000). However, as work such as that of White (1984) and Porciani et al. (2002) has shown, the non-linear effects inherent in the formation of large-scale structure lead to large quantitative disagreements between the predictions of the tidal torque theory and the angular momenta found in  $N$ -body simulations of dark matter haloes.

$N$ -body simulations provide the way to progress beyond the linear regime. As computing power has improved, so has the scale and resolution of simulations. Very early numerical studies of the angular momentum of “proto-galaxies” were performed by Peebles (1971) (with  $N_p \sim 100$  particles) and Efstathiou & Jones (1979) ( $N_p = 1000$ ), and led the way to the analysis of the spins and shapes of CDM haloes in more sophisticated simulations (Davis et al. 1985; Barnes & Efstathiou 1987; Frenk et al. 1988; all with  $N_p = 32\,768$ ). Warren et al. (1992) used a much larger simulation ( $N_p \sim 10^6$ ) and focused particularly on the details of the distributions of halo spins and shapes, and their relationship through the alignment of the halo angular momentum vector. Cole & Lacey (1996) also investigated the shapes and spins of dark matter haloes, in addition to various other aspects of halo structure.

An early study by Barnes & Efstathiou (1987) examined the relationship between spin and the spatial clustering of haloes, as measured by the two-point correlation function. Later, Lemson & Kauffmann (1999) examined the environmental dependence of halo properties, and found no correlations with halo spin. More recently, Faltenbacher et al. (2002) have carried out a mark correlation function analysis to investigate how spin varies with halo pair-separation. They found that neighbouring cluster pairs tend to have higher spins than the average.

Recent years have seen a large amount of work on the analysis of haloes in  $\Lambda$ CDM simulations. Halo shapes and their variation with mass were investigated by Bullock (2002), Kasun & Evrard (2005), Shaw et al. (2006) and Allgood et al. (2006). In agreement with previous studies, halo spin was found to vary little, if at all, with halo mass. The relationship between halo shape and spin was investigated by Bailin & Steinmetz (2005), Avila-Reese et al. (2005), Shaw et al. (2006) and Gottlöber & Turchaninov (2006). While this paper was being completed, independent analysis of halo properties, investigating halo concentrations, spins and shapes in a series of simulations, was posted by Macciò et al. (2006).

Using the the 10-billion particle Millennium simulation of the evolution of dark matter in the  $\Lambda$ CDM cosmology (Springel et al. 2005), we re-examine, in this paper, some of the shape and spin properties of dark matter haloes previously considered. Our analysis improves upon earlier work because the millions of haloes that formed in this simulation provide unprecedented statistical power. This allows us, for example, to quantify the distribution of halo spins and the relationship between spin, halo mass and shape with a precision that has not hitherto been possible. Unlike previous work, we consider different ways to identify haloes in the simulations; it turns out that the details of halo definition and selection can have a strong impact on the results. Finally we investigate how halo clustering depends on spin and shape for haloes of different masses.

This paper is structured as follows. Section 2 provides

|                         |                          |                                  |                       |      |            |
|-------------------------|--------------------------|----------------------------------|-----------------------|------|------------|
| $\Omega_\Lambda$        | $\Omega_M$               | $\Omega_b$                       | $h$                   | $n$  | $\sigma_8$ |
| 0.75                    | 0.25                     | 0.045                            | 0.73                  | 1.00 | 0.9        |
| $L_{\text{box}}$        | $N_{\text{part}}$        | $m_p$                            | $\eta$                |      |            |
| $500 h^{-1} \text{Mpc}$ | $2160^3 \approx 10^{10}$ | $8.6 \times 10^8 h^{-1} M_\odot$ | $5 h^{-1} \text{kpc}$ |      |            |

**Table 1.** Cosmological and simulation parameters for the Millennium Run. The first row describes the cosmology used. It gives the density parameters  $\Omega_i := \frac{\rho_i}{\rho_{\text{crit}}}$ , where the critical density  $\rho_{\text{crit}} := \frac{3H_0^2}{8\pi G}$  (with  $\rho_\Lambda := \frac{\Lambda}{8\pi G}$  and  $\Omega_{\text{tot}} = \Omega_\Lambda + \Omega_M = 1$ ), the Hubble parameter where  $H_0 = 100h(\text{km s}^{-1} \text{Mpc}^{-1})$ , the spectral index,  $n$ , and  $\sigma_8$ , the linear-theory power spectrum variance in spheres of radius  $8 h^{-1} \text{Mpc}$ . The second row gives the simulation parameters: the length of the side of the simulation cube, the number of particles, the resulting particle mass and the gravitational softening length. For further details, see Springel et al. (2005).

a description of the Millennium simulation itself, and the various halo properties we shall be investigating. Section 3 describes the construction of the catalogues whose haloes we investigate, including the group-finding algorithms and halo selection criteria. These we use to remove haloes whose properties are unreliable or biased, due to both numerical effects and the group-finding algorithms themselves. The main results of this paper are presented in §4, where we describe the distribution of halo spins as a function of mass and shape, and examine its effect on halo clustering. Our conclusions are presented in §5. Finally, the Appendix shows various examples of haloes that illustrate the effects of the group-finders.

## 2 DARK MATTER HALO PROPERTIES IN THE MILLENNIUM SIMULATION

### 2.1 The simulation

The Millennium simulation is described by Springel et al. (2005). It followed the evolution of 10 billion dark matter particles in the  $\Lambda$ CDM model, the standard paradigm of modern cosmology. This is strongly favoured by measurements of the temperature anisotropies in the microwave background radiation (Spergel et al. 2003, 2006) and by measurements of the clustering of galaxies (Percival et al. 2002; Tegmark et al. 2004; Sánchez et al. 2006). For reference, the key parameters of the simulation are listed in Table 1.

The simulation gives the positions and velocities of all particles at each “snapshot” in time; 64 snapshots are stored from the initial redshift ( $z = 127$ ) to the present, enabling redshift-dependent statistics to be studied.

### 2.2 Halo properties

For each halo-finding algorithm we consider in this paper, we compute a range of halo properties. We shall discuss these quantities here, and defer the details of the halo-finding and halo-selection algorithms to the next section.

Much of this work concentrates on the dimensionless spin parameter  $\lambda$ , introduced by Peebles (1969, 1971). This is defined as:

$$\lambda := \frac{J|E|^{1/2}}{GM_h^{5/2}} \equiv \frac{j|E|^{1/2}}{GM_h^{3/2}} \quad (1)$$

where  $M_h$  is the halo mass,  $J$  is the magnitude of the angular momentum vector  $\mathbf{J}$  (and  $j$  is the specific angular momentum),  $E$  is the total energy, and  $G$  is Newton's gravitational constant. It is important to note that  $\lambda$  is defined for any object which has a well-defined  $j$ ,  $E$  and  $M_h$ ; all these quantities are conserved for an isolated system, virialised or not. In reality, none of the haloes in cosmological simulations are completely isolated, leading to ambiguities in the definition. This means that for the  $\lambda$  of a halo to be useful, it is the definition of *halo* that requires the most care (and conditions such as virialisation; see section 3.2), not the definition of  $\lambda$ .

The meaning of  $\lambda$  is therefore best understood by considering an isolated, virialised, spherical system. The spin parameter can be seen to be a measure of the amount of coherent rotation in a system compared to random motions. For a spherical object, it is approximately the ratio of its own angular velocity to the angular velocity needed for it to be supported against gravity solely by rotation (see e.g. Padmanabhan 1993).

The specific angular momentum  $\mathbf{j}$  and kinetic energy  $T$  of each halo containing  $N_p$  particles are given by:

$$\mathbf{j} = \frac{1}{N_p} \sum_{i=1}^{N_p} \mathbf{r}_i \times \mathbf{v}_i \quad (2)$$

$$T = \frac{1}{2} M_h \sum_{i=1}^{N_p} \mathbf{v}_i^2 \quad (3)$$

where  $\mathbf{r}_i$  is the position vector of particle  $i$  relative to the halo centre, and  $\mathbf{v}_i$  is its velocity relative to the halo centre of momentum.

The halo potential energy,  $U$ , is calculated using all halo particles if  $M_h \leq 1000m_p$ , and is rescaled up from that of 1000 randomly-sampled particles otherwise. The potential is that used in the simulation itself:

$$U = \left( \frac{N_p^2 - N_{\text{sel}}}{N_{\text{sel}}^2 - N_{\text{sel}}} \right) \left( \frac{-Gm_p^2}{\eta} \right) \sum_{i=1}^{N_{\text{sel}}-1} \sum_{j=i+1}^{N_{\text{sel}}} -W_2(r_{ij}/\eta) \quad (4)$$

where  $N_{\text{sel}}$  is the number of selected particles ( $N_{\text{sel}} \leq 1000$ ),  $\eta$  is the softening length (see Table 1),  $r_{ij}$  is the magnitude of the separation vector between the  $i$ th and  $j$ th particles in the halo, and the softening kernel (see Springel et al. 2001) is:

$$W_2(u) = \begin{cases} \frac{16}{3}u^2 - \frac{48}{5}u^4 + \frac{32}{5}u^5 - \frac{14}{5}, & 0 \leq u \leq \frac{1}{2}, \\ \frac{1}{15u} + \frac{32}{3}u^2 - 16u^3 + \frac{48}{5}u^4, & \frac{1}{2} \leq u \leq 1, \\ -\frac{32}{15}u^5 - \frac{16}{5}, & \\ -\frac{1}{u}, & u \geq 1 \end{cases} \quad (5)$$

A halo's shape is derived from its mass distribution, which we characterise using the inertia tensor,  $\mathbf{I}$ . This relates angular momentum  $\mathbf{J}$  and angular velocity  $\boldsymbol{\omega}$  through  $\mathbf{J} = \mathbf{I}\boldsymbol{\omega}$ , and is formed from the following components:

$$I_{\alpha\beta} := \sum_{i=1}^{N_p} m_i (\mathbf{r}_i^2 \delta_{\alpha\beta} - r_{i,\alpha} r_{i,\beta}) \quad (6)$$

where  $\mathbf{r}_i$  is the position vector of the  $i$ th particle,  $\alpha$  and  $\beta$  are the tensor indices with values of 1, 2 or 3, and  $\delta_{\alpha\beta}$  is the Kronecker delta. The process of diagonalising  $\mathbf{I}$  is

equivalent to rotating the coordinate system to find a set of axes in which a torque about one does not induce a rotation about another; i.e. such that  $\mathbf{J}$  is parallel to  $\boldsymbol{\omega}$ . These axes then describe a hypothetical uniform ellipsoid whose axes  $a \geq b \geq c$  are those of the halo itself:

$$\mathbf{I} = \frac{1}{5} M_h \begin{pmatrix} b^2 + c^2 & 0 & 0 \\ 0 & a^2 + c^2 & 0 \\ 0 & 0 & a^2 + b^2 \end{pmatrix} \quad (7)$$

The eigenvalues are the moments of inertia  $\mathcal{I}$  for rotation about that axis. For example, rotation about the semimajor axis  $\mathbf{a}$  has the moment of inertia  $\mathcal{I}_a = \frac{1}{5} M_h (b^2 + c^2)$ ; note that  $\mathcal{I}_a \leq \mathcal{I}_b \leq \mathcal{I}_c$ . These eigenvalues can then be combined to find the relative axis lengths, e.g.

$$a = \sqrt{\frac{5}{2M_h} (-\mathcal{I}_a + \mathcal{I}_b + \mathcal{I}_c)} \quad (8)$$

The axis vectors are given directly by the corresponding eigenvectors, so that, for example, rotation about the  $\mathbf{a}$ -axis of the ellipsoid (with the longest length  $a$ ) has the smallest moment of inertia,  $\mathcal{I}_a$ .

Much of the literature on halo shapes uses the following description of the mass distribution, confusingly also calling it the inertia tensor (see, e.g. Cole & Lacey 1996, Hopkins et al. 2005, Bailin & Steinmetz 2005, Shaw et al. 2006):

$$\mathcal{M}_{\alpha\beta} = \frac{1}{N_p} \sum_{i=1}^{N_p} r_{i,\alpha} r_{i,\beta} \quad (9)$$

The results are entirely equivalent: if one diagonalises this matrix, then  $a$ ,  $b$  and  $c$  can be found as just the square roots of the eigenvalues, and the eigenvectors again give the axis vectors.

Once the halo's principal axes have been found, relationships between the axes and between the shape and other properties such as spin can be examined in terms of the axis ratios  $p := c/b$ ,  $q := b/a$  and  $s := c/a$ . The minor-to-major axis ratio  $s$  is a useful measure of the sphericity of the system, but does not specify in what way a halo might be aspherical. For this, we can use the triaxiality parameter introduced by Franx et al. (1991):

$$\mathcal{T} = \frac{a^2 - b^2}{a^2 - c^2} \quad (10)$$

This measures whether a halo is prolate ( $\mathcal{T} = 1$ ) or oblate ( $\mathcal{T} = 0$ ), but it does not quantify how aspherical a halo is.

## 3 THE HALO CATALOGUES

### 3.1 Groupfinder algorithms

The problem of how best to identify groups of particles within  $N$ -body simulations is a ubiquitous feature in studies of dark-matter halo properties. Many solutions have been found to this problem, typically involving first finding candidate-halo centres, followed by an iterative scheme to shrink or grow the halo according to criteria involving the binding energy or overdensity. Such algorithms include Bound Density Maxima (BDM, Klypin et al. 1999), Spline Kernel Interpolative DENMAX (SKID, Weinberg et al. 1997), the AMIGA Halo Finder (AHF, Gill et al. 2004), and SUBFIND (Springel et al. 2001), which we use below.

The very simple ‘friends-of-friends’ group-finder (FOF, Davis et al. 1985) was run on-the-fly, during the Millennium simulation run, with a linking length of  $s_0 = b(L_{\text{box}}^3/N_{\text{part}})^{1/3}$  where  $b = 0.2$ , to attempt to select virialised structures in the particle distribution. As is often the case (e.g. Porciani et al. 2002, Shaw et al. 2006, Macciò et al. 2006), this simple FOF catalogue forms the basis for the more sophisticated halo definitions we use.

An enhanced version of the SUBFIND program (Springel et al. 2005) was run on the data to identify self-bound substructures within each FOF halo, which we then use to construct the different group catalogues we investigate. The SUBFIND algorithm is essentially a two-step process. The first task is to identify subhalo candidates within each FOF halo. This is done using an adaptively-smoothed dark matter density field, effectively lowering a density threshold and identifying the peaks that grow out of it. The second stage consists of performing an iterative gravitational unbinding procedure on the candidates, successively removing particles that are not bound to the subhalo candidate. For this purpose, the potential energies are computed using a tree algorithm similar to that used for the simulation itself. The candidates that are left with at least 20 particles after this procedure are then subhaloes of the parent halo. The algorithm can and does identify subhaloes within subhaloes. It results in the FOF haloes typically consisting of a hierarchy of self-bound structures (which are not necessarily bound to each other), and a set of particles (referred to as “fuzz”) that are spatially linked to the halo but not part of any self-bound (sub)structure. The most massive “subhalo” (MMSH) typically contains most of the mass of the corresponding FOF object, and so is best regarded as the self-bound background halo itself, with the remaining subhaloes as its substructure.

In addition to finding the bound structures within haloes, SUBFIND also computes certain subhalo properties, which are then stored in the subhalo catalogue files. These include the location of the potential minimum, the ID number of the most bound particle, the mass (number of particles), and the half-mass radius. SUBFIND also computes and stores additional data related to each parent halo. Starting at the potential minimum of the MMSH of a halo, three radii are found: the first two are those where the density within them drops below  $200\rho_{\text{crit}}$  and  $200\bar{\rho}$ , to aid comparison with other work. The third is the virial radius proper, which uses the fitting formula of Bryan & Norman (1998) for spherical top-hat collapse in a flat ( $\Omega_{\Lambda} + \Omega_{\text{M}} = 1$ ) cosmology (see also Eke et al. 1996):

$$\frac{\rho}{\rho_{\text{crit}}} = 18\pi^2 + 82(\Omega_{\text{M}}(z) - 1) - 39(\Omega_{\text{M}}(z) - 1)^2 \quad (11)$$

This gives  $\rho/\rho_{\text{crit}} \approx 94$  at  $z = 0$ . Although these properties are associated with sets of grouped particles, SUBFIND does not restrict itself to these particles when computing them.

We will now describe the group catalogues whose halo properties we have investigated, and how they are built from the results of the FOF and SUBFIND algorithms. A key point which is used for each halo definition is that we take the halo centre to be at the potential minimum of the MMSH. For reference, Table 2 gives a list of each halo catalogue we will discuss, and the number of haloes they contain.

| Halo catalogue        | Number of haloes |                    |
|-----------------------|------------------|--------------------|
| FOF (without SUBFIND) | 17 709 121       | (‘raw’ catalogue)  |
| FOFall                | 15 494 624       | (87.5% of FOF raw) |
| FOFclean              | 1 332 239        | (8.60% of FOFall)  |
| SOall                 | 15 458 379       | (99.8% of FOFall)  |
| SOclean               | 1 239 494        | (8.02% of SOall)   |
| TREEall               | 17 041 498       | (110.0% of FOFall) |
| TREEclean             | 1 503 922        | (8.83% of TREEall) |

**Table 2.** Numbers of haloes in the halo catalogues defined in this paper. The “all” catalogues are the unfiltered results of the groupfinder algorithms described in sections 3.1.1, 3.1.2 and 3.2.2. The “clean” catalogues have been filtered as discussed in sections 3.2.3 and 3.2.4, with the quasi-equilibrium parameter  $Q = 0.5$  and the particle-number limit  $N_{\text{p}} \geq 300$ .

### 3.1.1 FOF haloes

The basic FOF algorithm, run as already described, results in 17 709 121 groups containing at least 20 particles, i.e. of mass  $\gtrsim 1.7 \times 10^{10} h^{-1} M_{\odot}$ , at redshift  $z = 0$ . The most massive group contained 4 386 162 particles ( $\approx 3.8 \times 10^{15} h^{-1} M_{\odot}$ ). Using this catalogue we can therefore identify dark matter haloes over a range of more than 5 orders of magnitude in mass, ranging from subgalactic clumps to the most massive clusters.

In practice, since we use the centre (potential minimum) of the MMSHs as the centres of the haloes themselves, we only use FOF haloes for which SUBFIND has found bound substructures. Haloes without substructure (and hence without an MMSH) are excluded from our base FOF catalogue. This has the effect of reducing the catalogue size by 12.5%, preferentially at lower masses. We shall refer to this catalogue as FOFall, and we will not discuss the larger raw FOF catalogue further.

### 3.1.2 SO haloes

The properties calculated by SUBFIND make it possible to construct a second halo catalogue, in which each halo consists of only the particles within  $R_{\text{vir}}$  of the centre of the MMSH of the corresponding FOF object (note that these particles do not have to be members of the FOF halo). Due to the way SUBFIND constructs the MMSH, this yields haloes whose definition is similar to those from a “spherical overdensity” algorithm (Lacey & Cole 1994), so we will refer to them as the SO haloes. We do not impose a lower limit on the number of particles comprising these objects; as a result, haloes can be identified with masses  $< 20m_{\text{p}}$  when their virial radii encompass fewer particles than their original FOF halo. This is simply a consequence of the algorithm employed; later examination of halo spins reveals the need for a much higher particle-number limit, as discussed in full in Section 3.2.4. This halo definition is similar, but not identical, to that used in Macciò et al. (2006).

### 3.2 Better halo catalogues

#### 3.2.1 Groupfinder problems

The FOF and SO group-finding algorithms have various well-documented drawbacks. Groupfinders such as SO which use the overdensity contained within a spherical region tend to impose a more spherical geometry on the resulting systems. Although this is not a problem for many objects, the algorithm can sometimes result in very unnatural-looking structures. An example is shown in figure A4. This compares a massive FOF halo with the corresponding SO object. The centre of mass of the FOF system is well separated from the minimum of the potential, and the halo is significantly elongated. This results, when growing a sphere around the potential minimum to form the SO halo, in the virial overdensity being reached sooner in one direction than another. The SO halo contains particles in low-density regions outside the FOF halo, and has a sharp cutoff in another direction when the FOF halo continues. The more ‘normal’ haloes, in the background, are much less affected.

The problems associated with the FOF groupfinder can be more extreme, and can affect a greater proportion of the haloes. One of the most commonly-cited problems (e.g. Gelb & Bertschinger 1994, Governato et al. 1997) is that well-resolved objects identified using the FOF algorithm are often at risk of becoming linked with neighbouring objects via tenuous bridges of particles. Low-mass particle bridges are usually extremely transient structures, being just a chance grouping of particles at that instant in time. The joining of two (or more) otherwise unrelated objects of similar mass in this way results in a very large velocity dispersion. Examining the halo in velocity-space will clearly show the multiple-object nature of the system. An example of a halo formed from objects joined by a tenuous bridge can be seen in Fig. A1.

Sometimes more massive haloes can be formed by the chaining together of somewhat smaller objects that are undergoing mergers or close flybys with their neighbours. Their multi-object composition can again be seen in velocity space as well as in real space, and although their connections are likely to be less transitory than in the case of a thin bridge, these objects are nevertheless well out of their equilibrium state, and so are unhelpful when trying to characterise the spins of typical dark matter haloes. See Fig. A2 for an example of a larger multi-object halo.

A similar effect is that of velocity contamination of small objects due to their proximity to more massive ones (see Fig. A3 for an example). Just as particles can form a bridge between passing haloes at the moment of the snapshot, so an individual particle orbit can take it within the linking length of a neighbouring halo, without forming enough of a bridge for the haloes themselves to be joined. The smaller halo will be contaminated by these interloper particles, which will have a quite different mean velocity to the halo’s own particles. This causes the mean velocity to be shifted away from that of the ‘original’ halo, and the resulting halo to have a much larger velocity dispersion than expected for an object of that mass. The massive neighbouring object will have a much higher velocity dispersion anyway, so will be unaffected by such effects.

To illustrate the effect that these problems have on the physical properties we calculate, we show the spin distribu-

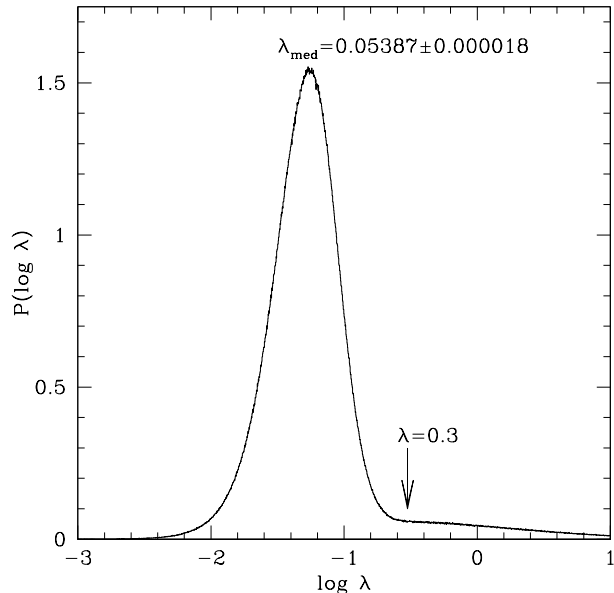


**Figure 1.** Histogram of the spin parameters from the basic FO-Fall halo catalogue of the Millennium Run, showing a long tail to high spins. The tail continues up to  $\lambda \approx 680$ , and there are over 900 000 objects with  $\lambda \geq 0.3$  (marked on the graph). The median spin of the distribution,  $\lambda_{\text{med}}$ , is displayed with the uncertainty given by Eqn. 13. This demonstrates the need for more careful definition and selection of haloes.

tion of the FO-Fall catalogue in Fig. 1. It shows a long tail at higher spins; there are 900 748 objects (6% of the catalogue) with spin  $\lambda \geq 0.3$ . Fig. 2 shows the FO-Fall spin distribution as a function of halo mass, rescaled to show the fractional number of objects at each mass so the trend of the mass function is removed. It shows that the high-spin tail comes from objects over a large range of masses, and is therefore not due to under-resolving groups. These presumed-anomalous high spins come from objects with high velocity dispersions for their masses, caused by situations such as those described above. This increases the haloes’ kinetic energies,  $T$ , leading to large values of  $\lambda$ .

These features are not usually seen in other published spin distributions (e.g. Gardner 2001, Vitvitska et al. 2002, Avila-Reese et al. 2005, Tonini et al. 2006, among many others), partly because more advanced groupfinders and halo selection criteria are often used (as we do below). However, the fact that we can see these artifacts so clearly is because the Millennium Run gives us a vast number of objects, over a wide range of masses.

For convenience, we shall refer to haloes suffering from the problems described in this subsection as ‘mis-defined’ haloes, as their anomalously-high spins originate in how the haloes are defined by the groupfinder algorithm in relation to their environment, rather than any physical or numerical effect.

#### 3.2.2 A better groupfinder: The TREE haloes

As a third definition of halo, we use the ‘merger-tree’ haloes described by Harker et al. (2006). These are the  $z = 0$  ob-

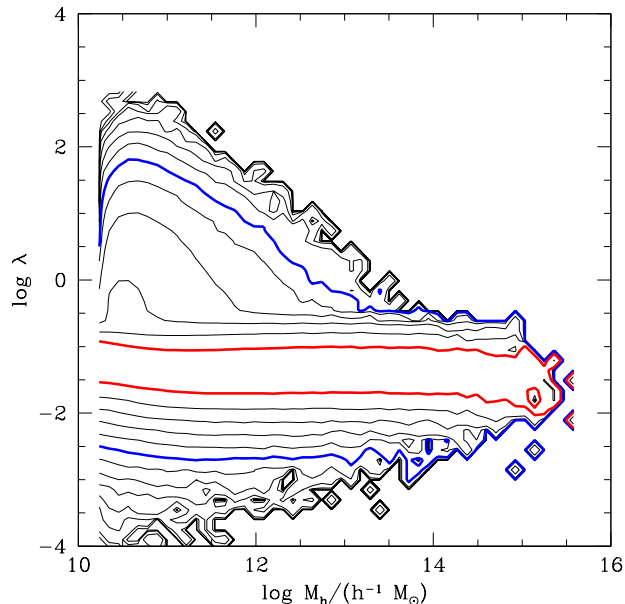


**Figure 2.** Halo spin as a function of halo mass for the FOFall halo catalogue. The contours indicate the relative number density of haloes with that value of  $\lambda(M_h)$ ; that is, the haloes were binned onto a  $50 \times 50$  grid between the maximum and minimum values in  $\log M_h$  and  $\log \lambda$ , and the number of haloes in each grid cell was normalised by the number of haloes in that mass-bin, thus removing the effects of the halo mass function from the plot. The contours are spaced logarithmically, with one contour for every factor of  $10^{0.5}$  in halo number density. The innermost bold contour (red) represents  $10^{-1}$  (i.e. a tenth of the haloes in each mass bin), and the outer bold contour (blue) represents  $10^{-3.5}$ . Notice the high-spin bulge, which extends over a large range of halo masses. The results for SO haloes show a very similar distribution.

jects in a catalogue of halo merger trees constructed in the Millennium Run (Helly et al., in preparation). These merger trees are similar to, but distinct from those of Springel et al. (2005) and Gao et al. (2005), who used different criteria for identifying and tracking the haloes over time. The merger-tree-halo catalogue used here was designed with the needs of the  $N$ -body GALFORM semi-analytic models in mind (e.g. Helly et al. 2003, Bower et al. 2006).

The haloes in the TREE catalogue are formed from the SUBFIND subhalo catalogue (based on the FOF haloes) in the following way. Each halo is initially taken to consist solely of its constituent subhaloes (i.e., is equivalent to the corresponding FOF halo, but without the “fuzz”). Next, a “splitting” algorithm is applied, which attempts to account for the linking of distinct, bound objects that often occurs with FOF. A subhalo can be split off from its parent halo if it satisfies at least one of the following conditions: 1) The distance between the subhalo’s centre and the parent’s centre is more than twice the parent’s half-mass radius; or 2) the subhalo has retained at least 75% of the mass it had at the last snapshot in which it was an independent halo. This second condition, which uses the merger-tree data, is based on the idea that if the subhalo was genuinely merging with the halo, it would be rapidly stripped of its mass. If however it was just a rapid encounter causing an artificial link, then

its mass would be retained. If the subhalo is split off, any other subhaloes that reside within twice *its* half-mass radius are also split off to become part of the new halo. We shall refer to the catalogue of all haloes defined in this method as the TREEall catalogue.

This definition of the TREE-halo catalogue alleviates the groupfinder-based problems somewhat. The unbound particles excluded from the TREE haloes have, by definition, higher velocities than the bound structures in the haloes. Their removal therefore reveals the more relaxed underlying haloes, with lower kinetic energies and hence  $\lambda$ . “Interloper particle” contamination, in particular, is reduced by this feature. The halo splitting algorithm also helps in many cases by separating objects that have been spuriously linked by bridges.

The spin-mass distribution of the TREEall catalogue can be seen in Fig. 3; although some of the high-spin objects remain, the majority are now gone (there are sufficiently few high-spin objects remaining that they are invisible in a plot of  $P(\log \lambda)$  such as Fig 2). Investigating the remaining high-spin objects reveals them to be victims of velocity contamination from very massive neighbours. They are somewhat special cases however: for them not to have been rejected as fuzz, the contaminants must be self-bound bodies, with  $\geq 20$  particles each. They must also be built on density maxima independent of that of the host halo, in order for SUBFIND to have identified them as separate subhaloes. Furthermore, the interloping subhalo must be within twice the half-mass radius of the halo, so that the tree algorithm does not split it off. A consequence of this is that the resulting halo must consist of at least 40 particles (20 for the interloper subhalo and 20 for the main halo), and this can be seen in the offset low-mass cutoff for high- $\lambda$  haloes in Fig. 3.

### 3.2.3 A better halo catalogue: The QE criterion

A relatively simple way of culling the remaining anomalous spin objects is to remove those that are clearly out of equilibrium at the moment of the snapshot. This is not quite the same as selecting only objects that are within a certain degree of true virialisation, since we don’t have the necessary time-resolution to determine if the system properties are genuinely stationary: just as an object can appear to be linked to another by a bridge that may exist only fleetingly, so a halo could instantaneously have very similar energies to those of a stationary system. Therefore we will apply a cut in the instantaneous ‘virial ratio’ of halo energies,  $2T/U + 1$ , and describe the objects that meet this criterion as haloes in a *quasi-equilibrium* (QE) state. This name avoids implying the zero time-derivative necessary for the true virial ratio.

The question of where to make the cut in ‘virialisation’ (i.e. applying a QE limit) is a difficult one, because the decision will always be somewhat arbitrary. Since it is desirable to minimise the effect of such arbitrariness, we concentrate on the effect of applying a QE limit to the TREE haloes, since the merger-tree algorithm has already removed many of the mis-defined haloes.

The value of  $2T/U + 1$  for the TREE haloes is plotted against their mass in Fig. 4. We applied a QE cut of the form

$$-Q \leq \frac{2T}{U} + 1 \leq Q \quad (12)$$

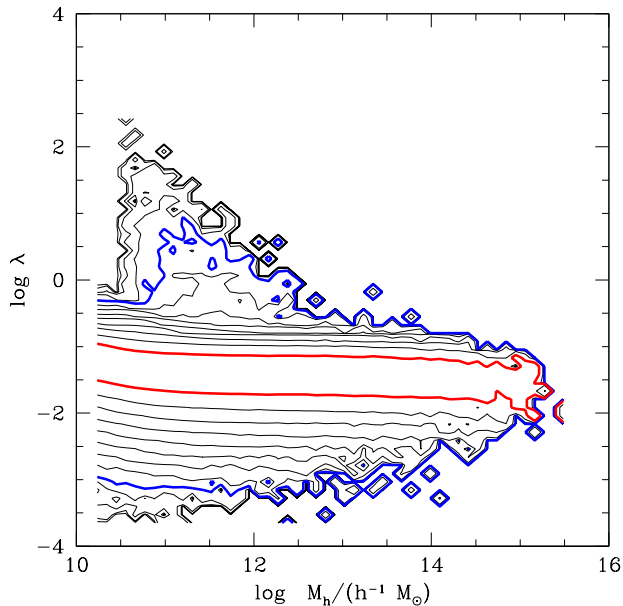


**Figure 3.** Spin as a function of halo mass for haloes in the TREEall catalogue. The contouring is as in Fig. 2, i.e. in equal logarithmic steps of  $10^{0.5}$ , normalised to remove the mass function. In this plot, the inner bold contour (red) represents  $10^{-1}$  of the haloes at each mass, and the outer bold contour (blue) represents  $10^{-5}$  of the haloes at each mass. The merger-tree halo definition has moved many of the high-spin haloes visible in Fig. 2 down into the main body of the distribution.

to the TREEall catalogue, examining the effect of a wide range of  $Q$ -values on the  $P(\log \lambda)$  and  $\lambda(M_h)$  distributions. Because of the relatively small numbers of objects with anomalously high spins, we find that the QE cut makes negligible difference to the shape of the spin distribution,  $P(\log \lambda)$ . A very small value,  $Q \lesssim 0.3$ , will act to shift the median spin lower by a few percent, due to the mass dependence seen in Fig. 4. Through a detailed examination of the  $\lambda(M_h)$  distribution, we find that a value of  $Q$  between 0.4 and 0.6 gives a good balance between removing the mis-defined haloes and reducing the overall sample size (adding noise and biasing it by mass). Higher values of  $Q$  allow some mis-defined haloes to creep in, with a significant impact for  $Q \gtrsim 1.0$ . We will use a value of  $Q = 0.5$  for our cleaned halo catalogues. This cut is shown in the horizontal dashed lines of Fig. 4, and the resulting  $\lambda(M_h)$  distribution is shown in Fig. 5. Applying this form of virialisation cut on the halo catalogue provides a useful tool with which to remove haloes with anomalous spins caused by mis-defined haloes.

### 3.2.4 A better halo catalogue: Numerical effects

A second peculiarity of the spin distributions is visible in Figs. 2, 3 and 5 (for the FOFall, TREEall and quasi-equilibrium TREE halo catalogues respectively): an upturn in the spin distribution at low masses. This can be seen clearer in the variation of the median spin over mass bins  $\lambda_{\text{med}}(M_h)$ , plotted for the FOF haloes in Fig. 6. This effect is unrelated to the velocity contamination problems of the mis-defined haloes, and instead comes from the mass resolu-

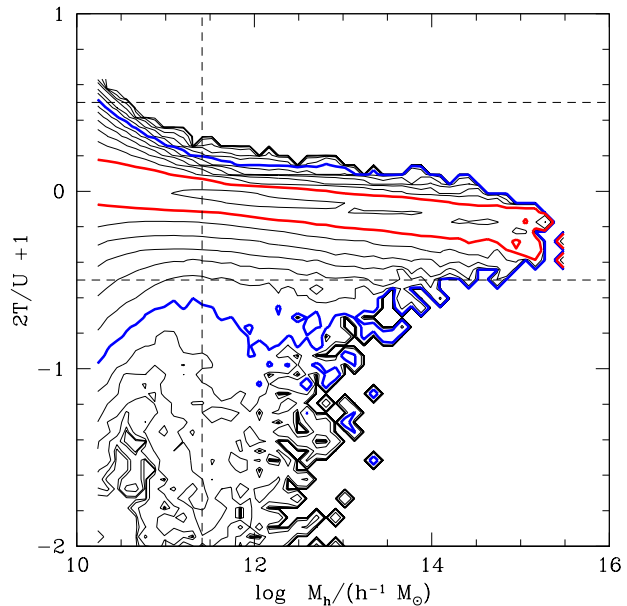


**Figure 4.** Contour plot of the instantaneous ‘virial ratio’,  $2T/U + 1$ , against halo mass for TREE haloes. A virialised object has a value around zero, and a gravitationally bound object has value  $> -1$ . The tail at low values (large  $T$ ) extends down to  $2T/U + 1 \approx -960$ ; there are 3733 objects with  $2T/U + 1 \leq -1$ . The dashed lines show the QE limit of  $Q = 0.5$ , and the lower particle-number limit of  $N_p = 300$ . The contouring is as in Fig. 2, i.e. relative halo number density in equal logarithmic steps of size  $10^{0.5}$ . The inner bold contour (red) represents  $10^{-1}$  of the haloes at each mass, and the outer bold contour (blue) represents  $10^{-4}$  of the haloes at each mass. The plots for FOF and SO groups are similar to this.

tion of the simulation affecting the angular momentum. This effect has been seen before, for example by Reed et al. (2005) in the context of subhaloes. To understand the cause of this effect, consider a continuous object with angular momentum  $\mathbf{J}_{\text{true}}$ . If we construct a realisation of this object using a sample of  $N$  discrete particles, the resulting angular momentum can be modelled as the vector sum of the ‘true’ angular momentum (from the continuous object) with a noise vector oriented in a random direction:  $\mathbf{J} = \mathbf{J}_{\text{true}} + \mathbf{J}_{\text{noise}}$ . This will act to push the measured magnitude  $J$  up above  $J_{\text{true}}$  because the random direction of  $\mathbf{J}_{\text{noise}}$  will mean it reaches outside the sphere of radius  $|\mathbf{J}_{\text{true}}|$  more than 50% of the time. Therefore, the random noise inherent in using discrete particles to sample a near-continuous object such as a dark matter halo would act to bias  $J$  upwards, and  $\lambda$  along with it.

Modern  $N$ -body codes such as the L-GADGET-II code used for the Millennium Run are very good at conserving quantities such as energy and angular momentum, so for a well-resolved object there is negligible inaccuracy arising from particle discreteness. For a less well-resolved object however, the effect can nevertheless be relevant, even though the angular momentum of the particles making up the halo has been well conserved. Discreteness mainly affects the outer parts of a halo, making the effective surface more jagged than that of the continuous object it represents. We also expect the outer parts to harbour most of the an-

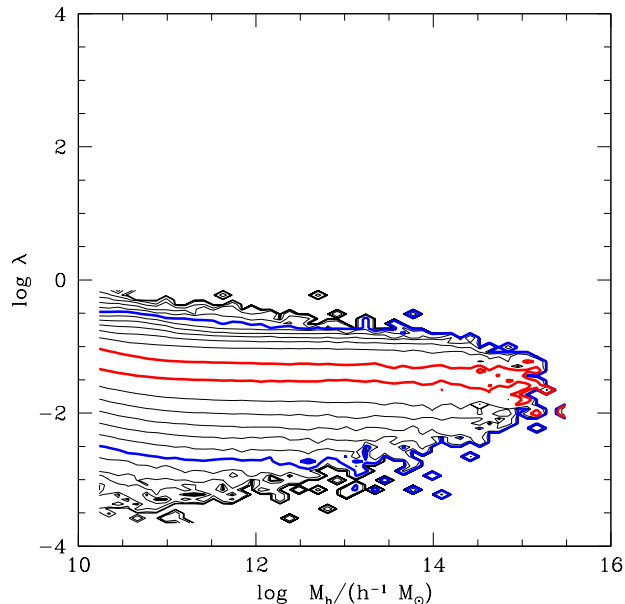


**Figure 5.** Spin parameter against halo mass for TREE haloes with a quasi-equilibrium (QE) limit of 0.5 applied; this can be compared with Figs 2 and 3. The same contouring is used, i.e. relative halo number density in equal logarithmic steps of size  $10^{0.5}$ . The inner bold contour (red) represents  $10^{-1}$  of the haloes at each mass, and the outer bold contour (blue) represents  $10^{-4}$  of the haloes at each mass. The QE-limit has removed the vast majority of the high-spin haloes seen in Fig. 3.

gular momentum. For lower-mass haloes, a greater fraction of their particles make up these ‘surface’ regions, so this problem has a greater effect; the inclusion of a single particle can make a significant contribution to  $\lambda$ . Hence, the spin parameter rises for haloes with fewer particles because the discreteness of the haloes’ surface layers adds noise to their ‘true’ angular momenta. (This is not the same effect as discussed in Shaw et al. (2006); there, a surface pressure term is added to the virial theorem to account for their halo truncation at  $R_{\text{vir}}$ .)

The importance of the noise contribution to  $\lambda$  can be examined by determining the spin distribution of the same simulation (same code and same corresponding initial condition waves) but ran at a different resolution. We performed a lower resolution resimulation of the Millennium Run, with  $2160^3/64 = 540^3$  particles (so their mass is  $m_{\text{p,low}} = 64m_{\text{p,Millen}}$ ), which we will refer to as *milli\_lowres*. The FOF and SUBFIND algorithms were implemented on *milli\_lowres* in the same way as in the Millennium Run itself. (Although we do not have merger-tree data for *milli\_lowres*, and hence cannot construct a TREE halo catalogue, the Millennium Run results show that the same effect is seen in FOF, SO and TREE haloes.) Fig. 6 shows the median spin  $\lambda_{\text{med}}(N_{\text{p}})$  for FOF haloes in the Millennium Run and *milli\_lowres*, with vertical error bars showing a Gaussian-like estimate of the precision of the median given by:

$$\epsilon_{\text{med}} := \frac{(\lambda_{84} - \lambda_{16})}{\sqrt{N_{\text{halo}}}} \quad (13)$$

where  $\lambda_i$  is the  $i$ th percentile of  $\lambda$  ( $84\% - 16\% = 68\%$ , the

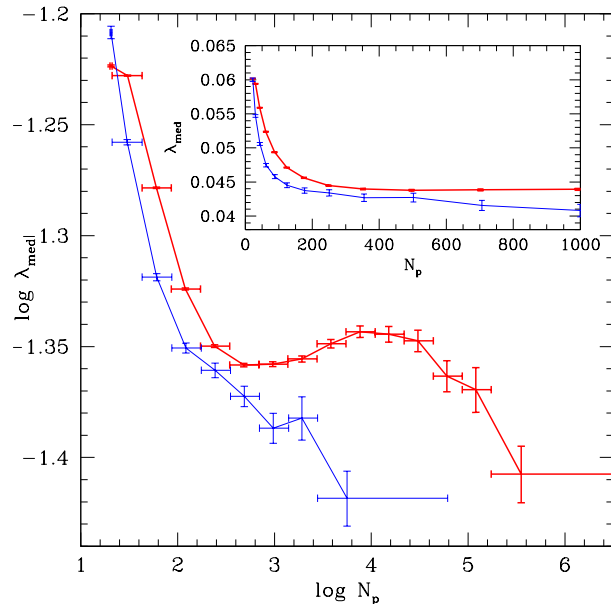


**Figure 6.** Median spins for all FOF haloes for the Millennium Run (thick red line) and the *milli\_lowres* run (thin blue line). The most massive bin contains 2000 haloes, and the remaining bins are logarithmically spaced, with one bin every factor of 2 in halo mass (except for the leftmost bin which extends down to the cutoff limit of 20 particles.) Horizontal bars mark the bin widths, and vertical error bars give a measure of the precision of the median according to Eqn. 13.

amount of data within  $\pm 1\sigma$  of a Gaussian peak) and  $N_{\text{halo}}$  is the number of haloes in that mass bin. Note that the *spread* in  $\lambda$  is much greater than the uncertainty in  $\lambda_{\text{med}}$ ; compare the error bars in Fig. 6 with the data shown in Fig. 2.

Although the two curves show the same qualitative behaviour (the low- $N_{\text{p}}$  upturn), there is a vertical shift between them. This is due to *milli\_lowres* containing fewer of the mis-defined objects described in Section 3.2.1 than the Millennium Run itself. Decreasing the resolution effectively smooths the density field, so that small objects with more massive neighbours can disappear completely, whereas a more isolated object of the same mass may still survive (although containing fewer particles). This means that the ‘real’ objects are retained (and there are still many under-resolved ones causing the upturn in  $\lambda_{\text{med}}(N_{\text{p}})$ ), but there is a reduction in the number of mis-defined objects. The *milli\_lowres* results seem to confirm the dominance of numerical effects at low- $N_{\text{p}}$ , above which the effect of noise is negligible.

If we apply the quasi-equilibrium cut described in section 3.2.3 to remove the mis-defined objects, we can examine the effect of discreteness on the median spins of just the ‘real’ haloes. Fig. 7 shows  $\lambda_{\text{med}}(N_{\text{p}})$  for QE-selected FOF haloes, compared with QE-selected FOF haloes from *milli\_lowres*. In contrast to Fig. 6, the two lines now lie on top of each other, exhibiting the same upturn in spin for haloes with the same number of particles. This demonstrates that the upturn is purely a numerical effect. We can exclude haloes that appear to be dominated by this effect by fixing a limit of  $N_{\text{p}} \geq 300$  on the halo catalogue.

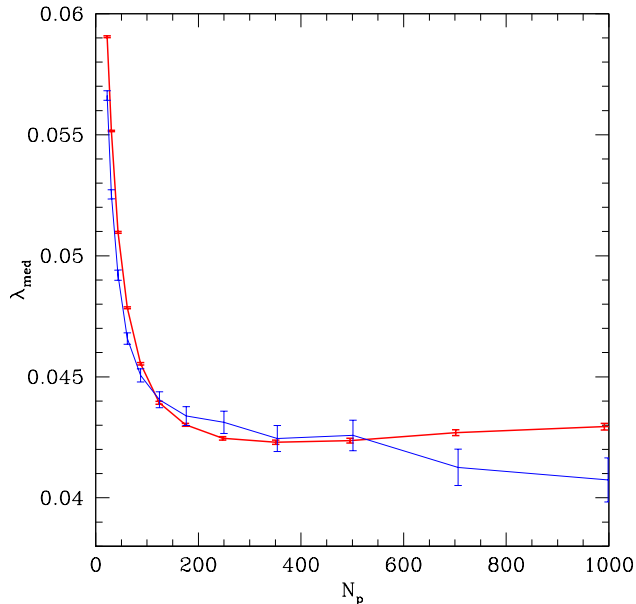


**Figure 7.** Median spins against number of particles in haloes, for FOF haloes with the QE cut applied. The thin blue line shows the `milli_lowres` haloes and the thick red line shows those from the Millennium Run itself. The error bars show the uncertainty on the median, using Eqn. 13. The two lines show an identical trend at low  $N_p$ , demonstrating that the upturn in  $\lambda_{\text{med}}$  is indeed a numerical effect, affecting the spins of haloes containing fewer than about 300 particles.

Fig. 4 shows how the QE and  $N_p$  cuts we use relate to one another for the TREE haloes. The low- $N_p$  cut has a significantly stronger effect on the halo catalogue. Applying the QE cut on its own reduces the population of the TREEall catalogue by only 0.3%; applying the low- $N_p$  limit as well means removing in total 91.17% of the original TREEall haloes (see Table 2). We refer to the resulting cleaned TREE-halo catalogue as TREEclean, and it is these haloes whose properties we shall be examining in detail. In some cases, for completeness, we shall compare the results with those from the FOFclean and SOclean catalogues. These are cleaned using the same  $Q = 0.5$  and  $N_p \geq 300$  cuts as the TREEclean catalogue.

It is important to note that the criteria we have adopted – the QE cut and low- $N_p$  limit – are those appropriate to the quantities of interest in this work. For example, Fausti-Neto et al (in prep.) use the substructure parameter  $S = \Delta r/R_{\text{vir}}$ , where  $\Delta r$  is the distance between the potential minimum of the halo and its centre of mass. Their final criteria for selecting haloes in the Millennium simulation are  $S < 0.07$  and  $\frac{2T}{U} + 1 > -0.25$ . They are concerned with fitting density profiles to haloes, and using the substructure parameter allows them to remove haloes with a large fraction of mass in substructures which would otherwise contaminate their results. Similarly, Macciò et al. (2006) define an “offset parameter” as  $x_{\text{off}} = \Delta r/R_{\text{vir}}$ , where  $\Delta r$  is measured from the most-bound particle rather than the potential minimum. They use this alongside the rms of their density profile fits, to assess the quality of their halo catalogues for estimates of halo concentration. Although we have examined the sub-

structure/offset parameter and how it affects  $\lambda$ , we find that it is not useful in removing the mis-defined haloes, or those whose spins are dominated by the numerical effects discussed above.

Having successfully implemented an appropriate groupfinder and cleaned the resulting halo catalogues, we can now proceed to examine their spin properties. The FOF and TREE halo catalogues, including some halo properties and semi-analytic galaxy properties, are publicly available online<sup>1</sup> (Lemson et al. 2006).

## 4 RESULTS

### 4.1 The form of the spin distribution

The median spin of the TREEclean halo catalogue is  $\lambda_{\text{med}} = 0.0381$ . The distribution of halo spins about the median,  $P(\lambda)$ , has been often fitted with a lognormal function (e.g. van den Bosch 1998; Gardner 2001; Bailin & Steinmetz 2005), i.e. a Gaussian in  $\log \lambda$ :

$$P(\log \lambda) = \frac{1}{\sigma_{1g}\sqrt{2\pi}} \exp\left[-\frac{\log^2(\lambda/\lambda_0)}{2\sigma_{1g}^2}\right] \quad (14)$$

While this fitting function has proved adequate for small numbers of objects, we find that for the  $> 10^6$  haloes in the Millennium simulation, deviations from a Gaussian are clear and significant. The spin distribution drops faster than a Gaussian at high spins, and slower than a Gaussian at low spins. The best fit to the TREEclean catalogue is shown in Fig. 8, which fits Eqn. 14 with peak location  $\lambda_0 = 0.03687 \pm 0.000016$  and width  $\sigma_{1g} = 0.2216 \pm 0.00012$ .<sup>2</sup> The corresponding lognormal function of  $\lambda$  has the same peak, and a width of  $\sigma = \ln(10)\sigma_{1g}$ . The fit has a reduced- $\chi^2$  of 40.46.

Part of the reason why a lognormal is such a poor fit is that this function strongly avoids very low spin values, whereas the real distribution, based as it is on the three-dimensional vector  $\mathbf{j}$ , does not. The longer tail at low- $\lambda$  is primarily due to the distribution of  $\mathbf{j}$  being smooth and isotropic about  $j = 0$ , implying<sup>3</sup> that  $P(\log \lambda) \propto \lambda^3$ .

We have found that the following function provides a better description of the data:

$$P(\log \lambda) = A \left(\frac{\lambda}{\lambda_0}\right)^3 \exp\left[-\alpha \left(\frac{\lambda}{\lambda_0}\right)^{3/\alpha}\right] \quad (15)$$

For the normalised spin distribution, we can express  $A$  in terms of the other free parameters,  $\alpha$  and  $\lambda_0$  (the peak location):

$$A = 3 \ln 10 \frac{\alpha^{\alpha-1}}{\Gamma(\alpha)} \quad (16)$$

<sup>1</sup> <http://www.mpa-garching.mpg.de/millennium/>

<sup>2</sup> Throughout this paper, the quoted uncertainties on best-fitting parameters are given by the square root of the diagonal of the covariance matrix for that fit.

<sup>3</sup> Macciò et al. (2006) claimed the low- $\lambda$  tail is due to the higher uncertainty in  $\lambda$  at low values. However, by varying the minimum  $N_p$  for the halo catalogue, and hence the uncertainty in  $\lambda$ , we found that the low- $\lambda$  side of the distribution consistently drops off slower than the high- $\lambda$  end, confirming that this shape is not primarily due to uncertainties.

where the gamma function  $\Gamma(\alpha) = (\alpha - 1)!$ . The best fit to the data is shown in Fig. 9, and has parameters:

$$\lambda_0 = 0.04326 \pm 0.000020 \quad \alpha = 2.509 \pm 0.0033$$

with a much-improved reduced- $\chi^2$  of 2.58.

We have examined whether the deviations from lognormal depends on our choice of the quasi-equilibrium parameter  $Q$  when cleaning the halo catalogue. We found that the fit remains good over a wide range of  $Q$ . We have also found the best fit of Eqn. 15 to the FOFclean and SOclean catalogues. The results for SOclean haloes are remarkably similar to those for the TREEclean haloes, with a reduced- $\chi^2$  of 3.10:

$$\lambda_0 = 0.04174 \pm 0.000022 \quad \alpha = 2.540 \pm 0.0036$$

The median spin of the distribution is  $\lambda_{\text{med}} = 0.0367$ . The haloes in the FOFclean catalogue, which have a median spin of  $\lambda_{\text{med}} = 0.04288$ , are not as well fitted by Eqn.15. The reduced- $\chi^2$  is 15.0 and the parameter values are:

$$\lambda_0 = 0.04929 \pm 0.000027 \quad \alpha = 3.220 \pm 0.0046$$

This is, in fact, slightly worse than the best-fitting lognormal (Eqn. 14), which yields a reduced- $\chi^2$  of 12.5, with a peak location  $\lambda_0 = 0.04222 \pm 0.000022$  and width  $\sigma_{\text{lg}} = 0.2611 \pm 0.00016$ .

These tests show that the distribution of  $\lambda$  depends on the careful definition and selection of dark matter haloes. However, the fact that the distribution is non-lognormal is not a consequence of the particular choice of groupfinder or selection criteria used here – the form of the distribution is not peculiar to the TREEclean catalogue.

## 4.2 Correlation of spin and halo mass

The variation of median spin parameter with halo mass, for the cleaned catalogues from the three groupfinders is shown in Fig. 10. It is interesting to note that the FOF haloes exhibit an upturn in spin for objects more massive than the low- $N_p$  cut, an effect that is not present in the TREE or SO haloes. This can be attributed to the outer parts of the FOF haloes consisting mainly of unbound ‘fuzz’ particles. These will usually have higher velocities, which act to inflate the spin. These particles are not part of the TREE haloes, and most will be shaved off in SO haloes too. The SO and TREE haloes show a shallow downwards trend of  $\lambda_{\text{med}}$  up to  $M_h \sim 10^{13} h^{-1} M_\odot \sim 12000 m_p$  and a rapid decline at larger masses.

We fit a cubic polynomial to the TREEclean median spin data,

$$\log \lambda_{\text{med}} = \alpha x^3 + \beta x^2 + \gamma x + \delta \quad (17)$$

where  $x = \log M_h / (h^{-1} M_\odot)$ . The best-fitting values of these parameters are:

$$\alpha = (-8.6 \pm 1.4) \times 10^{-3}$$

$$\beta = (3.2 \pm 0.54) \times 10^{-1}$$

$$\gamma = -4.1 \pm 0.68$$

$$\delta = 15.7 \pm 2.8$$

with a reduced- $\chi^2$  of 0.44.

While the trend of  $\lambda_{\text{med}}$  with mass is real, it is important to note that it is a small effect; the scatter around this

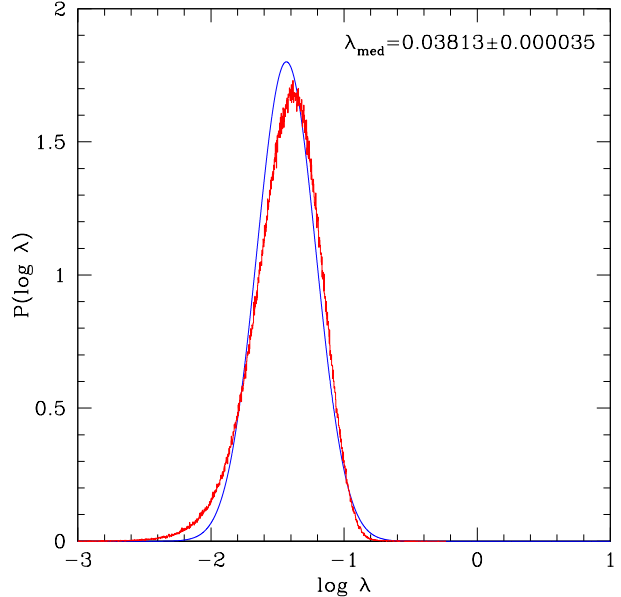


**Figure 8.** The normalised spin distribution (red histogram) for merger-tree haloes with  $N_p > 300$  and filtered using the QE criterion (the TREEclean catalogue). The best-fitting single Gaussian function is plotted as the smooth blue curve. The Gaussian drops too quickly at low spins, and too slowly at higher spins. To try to minimise these effects, the best fit has a peak location that is shifted away from that of the histogram data. The median spin of the distribution is also displayed.

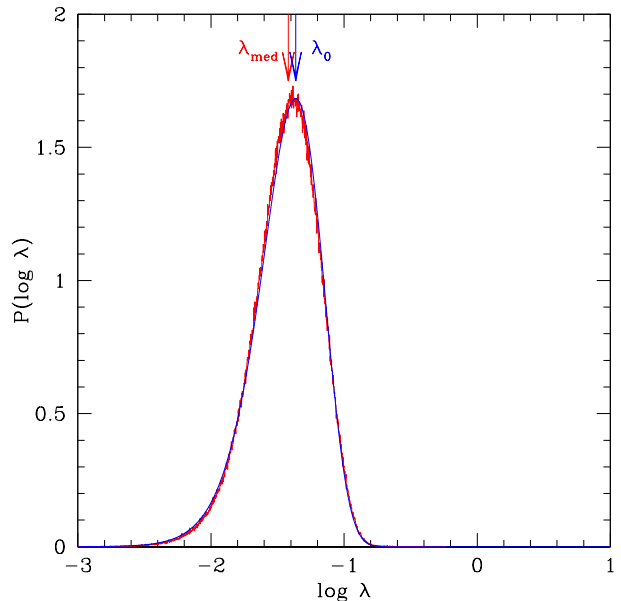


**Figure 9.** Histogram (red) of the normalised  $\log \lambda$  distribution of TREEclean haloes, as in Fig. 8. The smooth solid curve (blue) is the best fit to the data using Eqn 15. The peak location of the fit ( $\lambda_0$ ) and the median of the data ( $\lambda_{\text{med}}$ ) are marked with arrows.

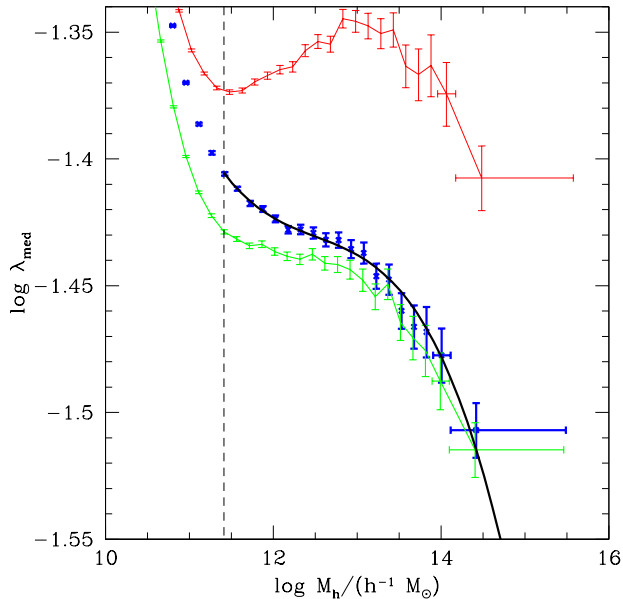


**Figure 10.** The median spins of halo mass bins, for TREEclean haloes (bold blue points), SOclean haloes (medium green line) and FOFclean haloes (thin red line). Data have also been calculated below the 300-particle low-mass limit (marked with a dashed line). The thick black curve is the best-fitting cubic polynomial to the TREEclean data. The vertical error bars are given by Eqn 13. The mass-binning scheme is similar to Fig. 6, but with bins every factor of  $\sqrt{2}$  in mass. Only the widths of the most massive two bins are marked, for clarity.

median is large (compare with Fig. 5, which shows data from the same haloes but on a  $\log \lambda$  scale). This is in qualitative agreement with previous results (e.g. Cole & Lacey 1996), but because of its weak nature, this trend has often not been visible (e.g. Warren et al. 1992; Lemson & Kauffmann 1999; Macciò et al. 2006).

### 4.3 The halo shape distribution

The shapes of the haloes are described by the axes,  $a \geq b \geq c$ , of the ellipsoid derived from the inertia tensor, as described in Section 2.2. Fig. 11 shows the distributions of  $p = c/b$  and  $q = b/a$  for the three cleaned halo catalogues. The haloes are generally triaxial, but they have a range of shapes, with a slight preference for prolateness over oblateness. The distribution agrees qualitatively with previous work such as that by Frenk et al. (1988), Warren et al. (1992), Cole & Lacey (1996), Faltenbacher et al. (2002) and Bailin & Steinmetz (2005). Unsurprisingly, SO haloes are more spherical than FOF or TREE haloes. FOF haloes show a much broader distribution of shapes (and a stronger preference for prolateness) than SO or TREE haloes.

Fig. 12 shows how the median shape of haloes in the TREEclean catalogue changes with halo mass, using the minor-to-major axis ratio  $s$  and the triaxiality parameter  $\mathcal{T} = (a^2 - b^2)/(a^2 - c^2)$ . More massive haloes tend to be less spherical and more prolate. Again, this is in qualitative agreement with previous results, such as those of Warren et al. (1992), Bullock (2002), Kasun & Evrard (2005),

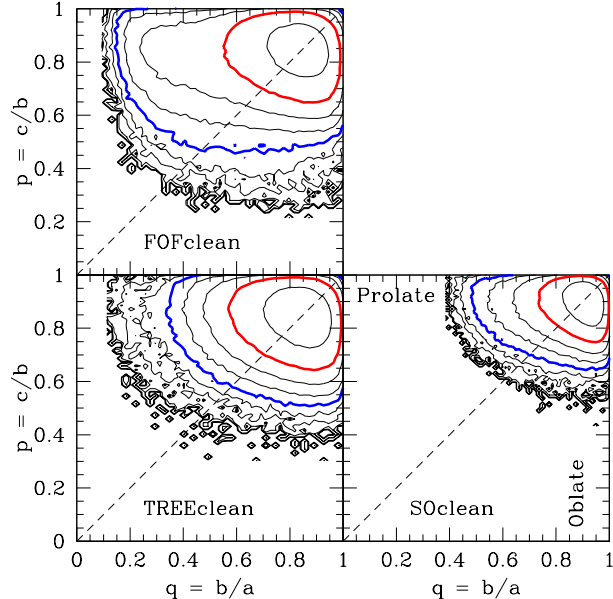


**Figure 11.** Axis ratios  $p$  and  $q$  for the cleaned TREE, FOF and SO halo catalogues. Prolate objects have  $p = 1$ , oblate objects have  $q = 1$ , and spherical objects have  $p = q = 1$ . The SO haloes are more spherical than the other two types. TREE and FOF objects exhibit a range of shapes, and all three catalogues show a preference for prolateness over oblateness. The contouring is by halo numbers, in equal logarithmic steps of  $10^{0.5}$ . In each plot, the red inner bold contour represents  $10^3$  haloes, and the blue outer bold contour represents  $10^{1.5}$  haloes.

Shaw et al. (2006), Gottlöber & Turchaninov (2006), Allgood et al. (2006), and Macciò et al. (2006). This is also what one might expect in a hierarchical formation model in which haloes tend to form by matter collapsing along filaments, leading to prolateness, rather than onto sheets which would lead to oblateness. Furthermore, the more massive haloes form later, and have had less time to relax into more spherical configurations. Since we have deliberately tried to select the more relaxed objects, the remaining trend we see here is weak. Furthermore, although the medians follow well-defined trends, the spread of the distribution in halo shapes covers virtually the entire range in both  $s$  and  $\mathcal{T}$ , as can be seen from the percentile bars on the graph.

The two graphs in Fig. 12 both show a change in behaviour not seen in previous work, around the  $N_p = 300$  limit. Resolution tests similar to those described in section 3.2.4 were carried out using the `milli_lowres` simulation, to assess whether this change in behaviour was indeed a numerical effect similar to that seen in halo spins (in Figs. 6, 7 and 10). The results showed that these halo shape parameters do also require  $N_p \gtrsim 300$ , reinforcing our previous choice. Indeed, one would expect haloes whose spins are affected by particle discreteness (i.e. with  $N_p \lesssim 300$ ) to be less spherical and more stringy (prolate).

We fit a broken line to both shape parameters for the TREEclean catalogue, of the form:

$$y_{\text{med}}(x) = \begin{cases} m_1 x + c_1 & x \leq x_0 \\ m_2 x + c_2 & x \geq x_0 \end{cases} \quad (18)$$

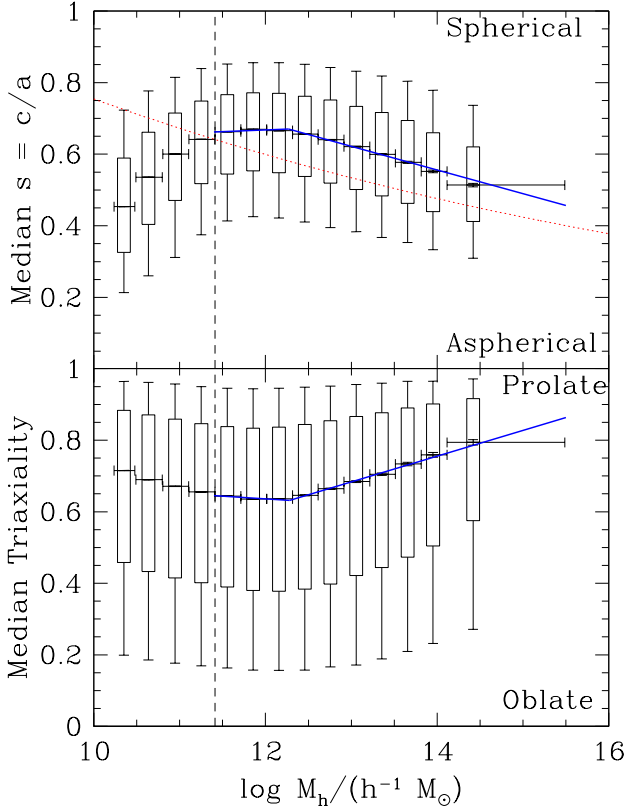


**Figure 12.** The median, in bins of halo mass, of the axis ratio  $s$  (top) and the triaxiality parameter  $\mathcal{T}$  (bottom), for TREEclean haloes, using the same mass binning scheme as in Fig. 6. The low- $N_p$  limit of 300 particles is marked with a dashed line, and data points have also been plotted below this limit). The medians for FOFclean and SOclean haloes follow the same behaviour as the TREEclean haloes, but with SO objects being more spherical and FOF objects less; FOF haloes are more prolate and SO haloes show a weaker preference for prolateness. Error bars on the medians (following Eqn. 13) are plotted, but most are vanishingly small. The whisker bars are percentiles, at the equivalent of  $1\sigma$  (68% of haloes, boxes) and  $2\sigma$  (95% of haloes, bars); from the bottom to the top of each graph, these show where approximately 2.5%, 16%, 84%, and 97.5% of the haloes have  $s$  (or  $\mathcal{T}$ ) below these values. The thick blue lines show broken-line fits to the data; see the text for details. The dotted red line is the fit of Allgood et al. 2006, who used a different definition of a halo (see text).

where  $x = \log M_h / (h^{-1} M_\odot)$ . We fit with  $m_1, m_2, x_0$  and  $c_2$  as free parameters, with  $c_1 \equiv c_2 + (m_2 - m_1)x_0$ . The fitted parameters for  $s_{\text{med}}$  are:

$$\begin{aligned} m_{1,s} &= (9.2 \pm 0.87) \times 10^{-3}, & c_{1,s} &= 0.56 \pm 0.015, \\ m_{2,s} &= (-6.6 \pm 0.12) \times 10^{-2}, & c_{2,s} &= 1.48 \pm 0.015, \\ x_{0,s} &= 12.27 \pm 0.012 \end{aligned}$$

with a reduced- $\chi^2$  of 29.9. The fitted parameters for  $\mathcal{T}_{\text{med}}$  are:

$$\begin{aligned} m_{1,\mathcal{T}} &= (-1.6 \pm 0.18) \times 10^{-2}, & c_{1,\mathcal{T}} &= 0.82 \pm 0.031, \\ m_{2,\mathcal{T}} &= (7.2 \pm 0.24) \times 10^{-2}, & c_{2,\mathcal{T}} &= -0.25 \pm 0.029, \\ x_{0,\mathcal{T}} &= 12.28 \pm 0.021 \end{aligned}$$

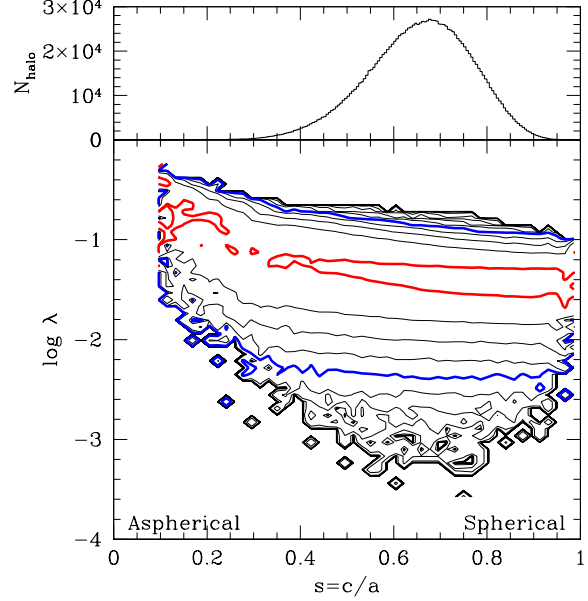


**Figure 13.** The main plot shows spin versus axis ratio  $s = c/a$  for TREEclean haloes; contouring is similar to Fig. 2, showing the number density of haloes, normalised by the number of haloes in each  $s$ -bin. The red inner bold contour represents  $10^{-1}$  of the haloes in each  $s$ -bin, the blue outer bold contour represents  $10^{-3}$  of the haloes in each  $s$ -bin, and the contours are spaced in equal logarithmic steps of  $10^{0.5}$ . The upper plot is a histogram of  $s$  for TREEclean haloes, effectively showing the function by which the contour plot has been normalised.

with a reduced- $\chi^2$  of 4.27. The two mass breakpoints  $x_{0,s}$  and  $x_{0,\mathcal{T}}$  agree within their uncertainties.

Allgood et al. (2006) fit a power-law to  $s_{\text{med}}(M_h)$ . This is plotted in Fig. 12, and indicates that their haloes are significantly less spherical than ours. This is largely a result of different group definitions; although not plotted, we find that our SOclean and FOFclean catalogues differ from the TREEclean results by a similar amount. A power-law of the type used by Allgood et al. (2006) would not be a good fit to the data presented here which have a definite change in slope towards lower halo masses.

The overall distributions of  $s$  and  $\mathcal{T}$  are shown in the upper plots of Figs. 13 and 15. These agree well with distributions seen previous work, e.g. Bailin & Steinmetz (2005) and Shaw et al. (2006). The drop-off in halo sphericity below about  $s \sim 0.3$  can be explained by considering how flatter haloes would puff up due to bending instabilities (Merritt & Sellwood 1994).

#### 4.4 Spin and shape parameters

The relationship between spin parameter and halo shape is illustrated in Figs 13, 14 and 15. Fig. 14 emphasises the trend visible in Fig. 13 by plotting the median spin parameter as a function of  $s$  for different mass bins. There is a clear trend for more spherical haloes to exhibit less coherent rotation. Although this trend is in the sense one might naively expect, the haloes, in fact, do not have very high spin, and are not rotationally supported. The origin of this trend is

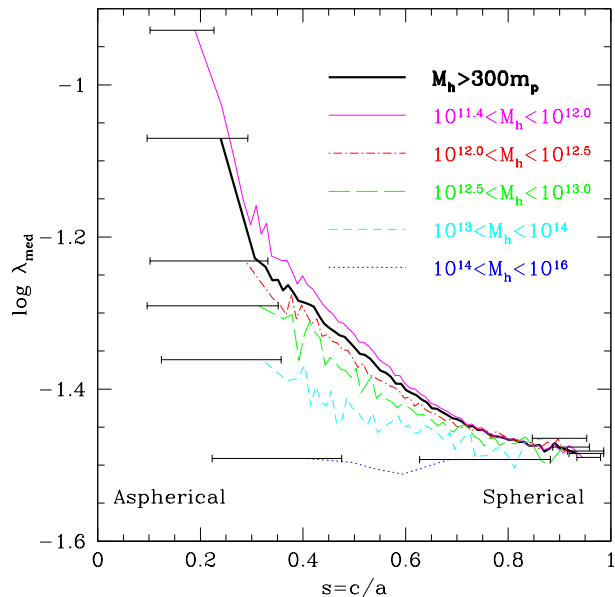


**Figure 14.** The median spin parameter in bins of axis ratio  $s = c/a$ , for haloes from the TREEclean catalogue. The heavy black line is for all haloes with more than 300 particles (the full TREEclean sample); the other lines show the trends for different halo mass bins. The horizontal bars show the widths of the first and last bins for each line. The trend is for more spherical haloes to have less coherent rotation in the median. This trend becomes very steep for the most aspherical haloes (although these are not present at higher masses because of the rapid drop in the halo mass function).

likely to lie instead in the effects of the tidal torques experienced by the haloes during their early phases of formation.

As seen previously in Fig. 10, the least massive objects have the most extreme spins, in the median. Fig. 14 shows that the higher spin objects are also less spherical. The haloes which are closest to spherical have a spin parameter that is independent of halo mass, and has  $\lambda_{\text{med}} \approx 0.033$ . (This does not apply to the most massive haloes, however, since their population lacks the more spherical objects) Furthermore, the median spins for the more massive haloes are independent of shape and have  $\lambda_{\text{med}} \approx 0.032$ .

In contrast to the variation of  $\lambda_{\text{med}}$  with  $s$ , Fig. 15 shows that there is only a very weak trend of spin with halo triaxiality. Over the entire range of triaxiality, each  $\mathcal{T}$ -bin contains a very similar fraction of haloes at each value of  $\log \lambda$ .

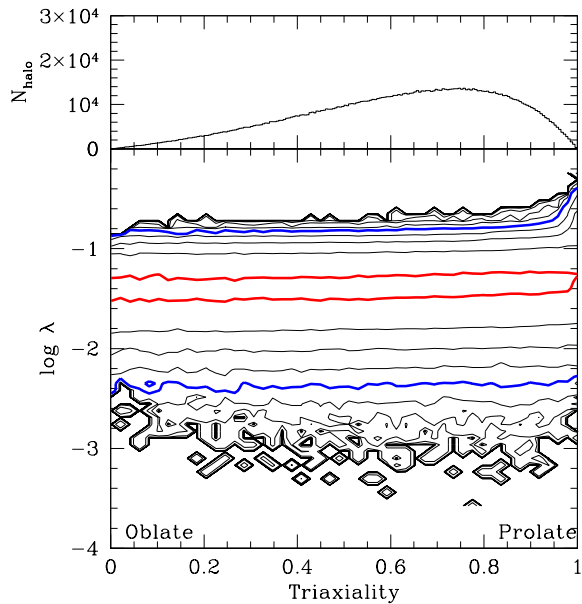
#### 4.5 Spin-shape alignment

Fig. 16 shows the angle between the angular momentum vector and the three shape axis vectors, e.g.:

$$\cos \theta_a = |\mathbf{j} \cdot \hat{\mathbf{a}}/j| \quad (19)$$

for alignment with the semimajor axis given by the unit vector  $\hat{\mathbf{a}}$ . Note that this definition does not distinguish between  $\mathbf{j}$  lying parallel or antiparallel to the axis vectors.

Most haloes have their spin axis well aligned with their minor axis, and lying perpendicular to their major axis. However, the distribution of alignments with respect to all



**Figure 15.** The main plot shows spin versus triaxiality parameter  $\mathcal{T}$  for TREEclean haloes; contouring is as for Fig. 13, i.e. in equal logarithmic steps of  $10^{0.5}$  haloes per  $\mathcal{T}$ -bin. The red inner bold contour represents  $10^{-1}$  of the haloes in each  $\mathcal{T}$ -bin, and the blue outer bold contour represents  $10^{-3}$  of the haloes in each  $\mathcal{T}$ -bin. The upper plot is a histogram of  $\mathcal{T}$  for TREEclean haloes, effectively showing the function by which the contour plot has been normalised.

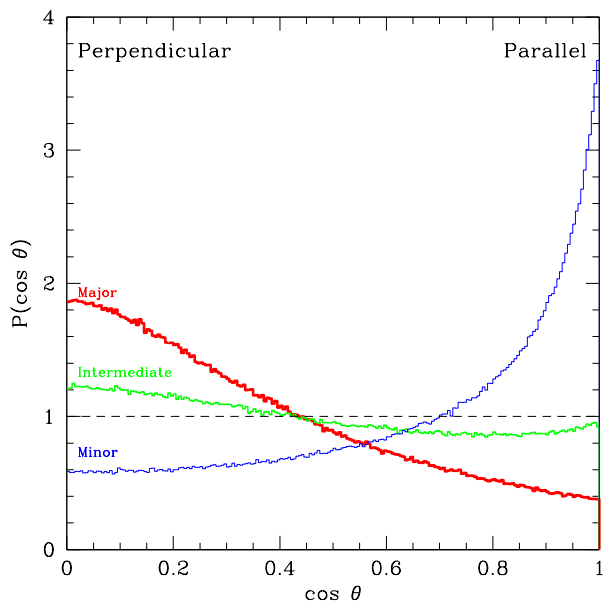


**Figure 16.** Normalised histograms of the cosines of the angle between the angular momentum vector and the major (thick red line), intermediate (medium green line) and minor (thin blue line) axes of haloes in the TREEclean catalogue, as defined in the text. A random distribution would be a flat line at  $P(\cos \theta) = 1$ .

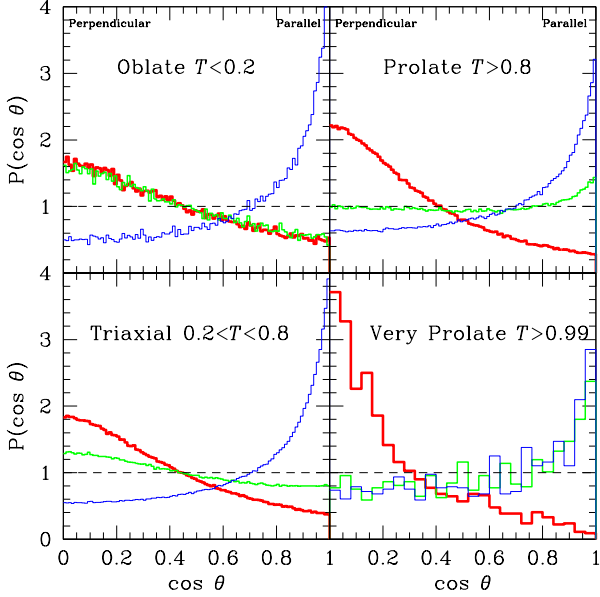


**Figure 17.** Normalised histograms of the cosine of the angle between the specific angular momentum vector and the major (thick red line), intermediate (medium green line) and minor (thin blue line) axes of the haloes. The TREEclean catalogue has been cut at the values of the triaxiality parameter shown. The most spherical haloes ( $s > 0.8$ ) have been removed from each sample. The ‘very prolate’ selection only contains 1360 groups, giving rise to a noisier histogram.

three axes is fairly broad. This agrees with previous results (e.g. Warren et al. 1992, Bailin & Steinmetz 2005, Allgood et al. 2006 and Shaw et al. 2006).

Extremely oblate objects have a degeneracy between the major and intermediate axes ( $\frac{b}{a} \sim 1$ ), so there is an equal probability for the angular momentum vector to subtend a given angle with either axis. This can be seen in the top-left panel of Fig. 17, which shows the alignment distribution for the more oblate haloes, i.e. those with  $\mathcal{T} < 0.2$  (and  $s < 0.8$  in order to avoid an  $a \sim b \sim c$  degeneracy). Since most haloes have  $\mathbf{j}$  aligned with  $\hat{\mathbf{e}}$ ,  $\mathbf{j}$  has a preference for being at right angles to the two large axes.

For extremely prolate haloes, the degeneracy is between minor and intermediate axes ( $\frac{c}{b} \sim 1$ ). In this case, the distribution of the alignment of the angular momentum vector with either of these axes is similar only for the tail of extremely prolate haloes,  $\mathcal{T} > 0.99$  (bottom-right panel). For  $\mathcal{T} > 0.8$ , only a small number of haloes have their spin axis aligned with the intermediate axis (top-right panel); like the bulk of the population as a whole, most of these haloes rotate around their smallest axis.

The reason for the distinction between the major and intermediate axes present in Fig. 16 can now be seen to be a combination of various effects. The preference for prolateness over oblateness means that there is a tendency for the intermediate axis to be more similar to the minor than to the major axis. This increases the probability of  $\mathbf{j}$  being aligned to the  $\hat{\mathbf{b}}$  axis. However, since  $\mathbf{j}$  can be aligned with only one axis (and when this happens it must be perpendicular to the other two), the preference for the spin axis to

be the minor axis outweighs the preference for prolateness, and this results in the slight excess probability for  $\mathbf{j}$  to be perpendicular to the intermediate axis seen in the figure.

#### 4.6 Spin, shape and Halo clustering

In this section, we investigate whether halo spin and shape has an environmental dependence. We quantify environment by means of the haloes’ two-point correlation function,  $\xi(r)$ , and we explore whether the clustering amplitude differs for haloes with different spin. The three halo catalogues were divided into four bins in mass, and the haloes in each mass bin were then divided about the median spin for that mass;  $\xi(r)$  was calculated for each set of haloes. The results are plotted in Figs 18 and 19 for the TREEclean and FOFclean catalogues respectively. (The results for SOclean haloes are very similar to the FOF results.) The lines in Fig. 18 show power-law fits over the limited range of pair separations shown,

$$\xi(r) = \left(\frac{r}{r_0}\right)^\gamma. \quad (20)$$

The fitted values of  $r_0$  and  $\gamma$  are given in Table 3.

For the higher mass bins, the results from the different types of haloes are similar: higher spin haloes are more strongly clustered than lower spin haloes. This could be because objects evolving in denser, more clustered environments are more likely to experience stronger tidal forces, leading to more coherent rotation. These results are consistent with the tentative earlier work of Barnes & Efstathiou (1987), as well as the mark correlation function analysis of Faltenbacher et al. (2002)

The difference in clustering strength between high and low spin haloes decreases with halo mass. For the least massive TREE haloes,  $M = 10^{11.4} - 10^{12} h^{-1} M_\odot$ , there is virtually no difference in the correlation functions of the fast and slow rotators.

Note that haloes from the ‘cleaner’ groupfinder (TREE) exhibit stronger clustering at all scales, for all but the highest masses. This is due to the fact that the splitting algorithm applied during the construction of the merger trees results in a greater number of close halo neighbours (albeit with reduced masses) compared to the corresponding FOF haloes.

We have performed a similar analysis to that presented in Figs. 18 and 19 for the halo sphericity parameter,  $s$ . We found analogous results, in that the more spherical haloes are more clustered than the less spherical haloes.

To examine the effect of halo spin and shape on clustering in more detail, we consider the bias parameter,  $b$ , which describes how much more or less clustered a set of haloes is relative to the underlying dark matter distribution. We examine how the bias varies for haloes with different values of  $\lambda$  or  $s$ , at a fixed range of mass. Similar analyses have recently been performed by Gao et al. (2005), Wechsler et al. (2005) and Wetzel et al. (2006), who examined the effect of halo formation time, concentration, substructure content and time since last major merger on the bias.

The bias parameter is related to the correlation function through:

$$\xi_{\text{hh}}(r|M_{\text{h}}, \lambda) = b^2(r|M_{\text{h}}, \lambda)\xi_{\text{mm}}(r) \quad (21)$$

| Mass bin<br>( $h^{-1}M_{\odot}$ ) | $\lambda < \lambda_{\text{med}}$ |                          | $\lambda \geq \lambda_{\text{med}}$ |                          |
|-----------------------------------|----------------------------------|--------------------------|-------------------------------------|--------------------------|
|                                   | $\gamma$                         | $r_0/(h^{-1}\text{Mpc})$ | $\gamma$                            | $r_0/(h^{-1}\text{Mpc})$ |
| $10^{11.4}-10^{12}$               | $-1.553 \pm 0.0013$              | $3.670 \pm 0.0070$       | $-1.489 \pm 0.0012$                 | $3.671 \pm 0.0073$       |
| $10^{12}-10^{13}$                 | $-1.591 \pm 0.0031$              | $4.22 \pm 0.020$         | $-1.537 \pm 0.0026$                 | $4.82 \pm 0.021$         |
| $10^{13}-10^{14}$                 | $-1.64 \pm 0.021$                | $6.6 \pm 0.24$           | $-1.71 \pm 0.016$                   | $8.3 \pm 0.23$           |
| $10^{14}-10^{16}$                 | $-1.6 \pm 0.19$                  | $13 \pm 5.8$             | $-1.7 \pm 0.12$                     | $19 \pm 4.8$             |

**Table 3.** Parameters for the power-law  $\xi(r) = (r/r_0)^\gamma$  from fitting to the eight two-point correlation functions for TREEclean haloes.

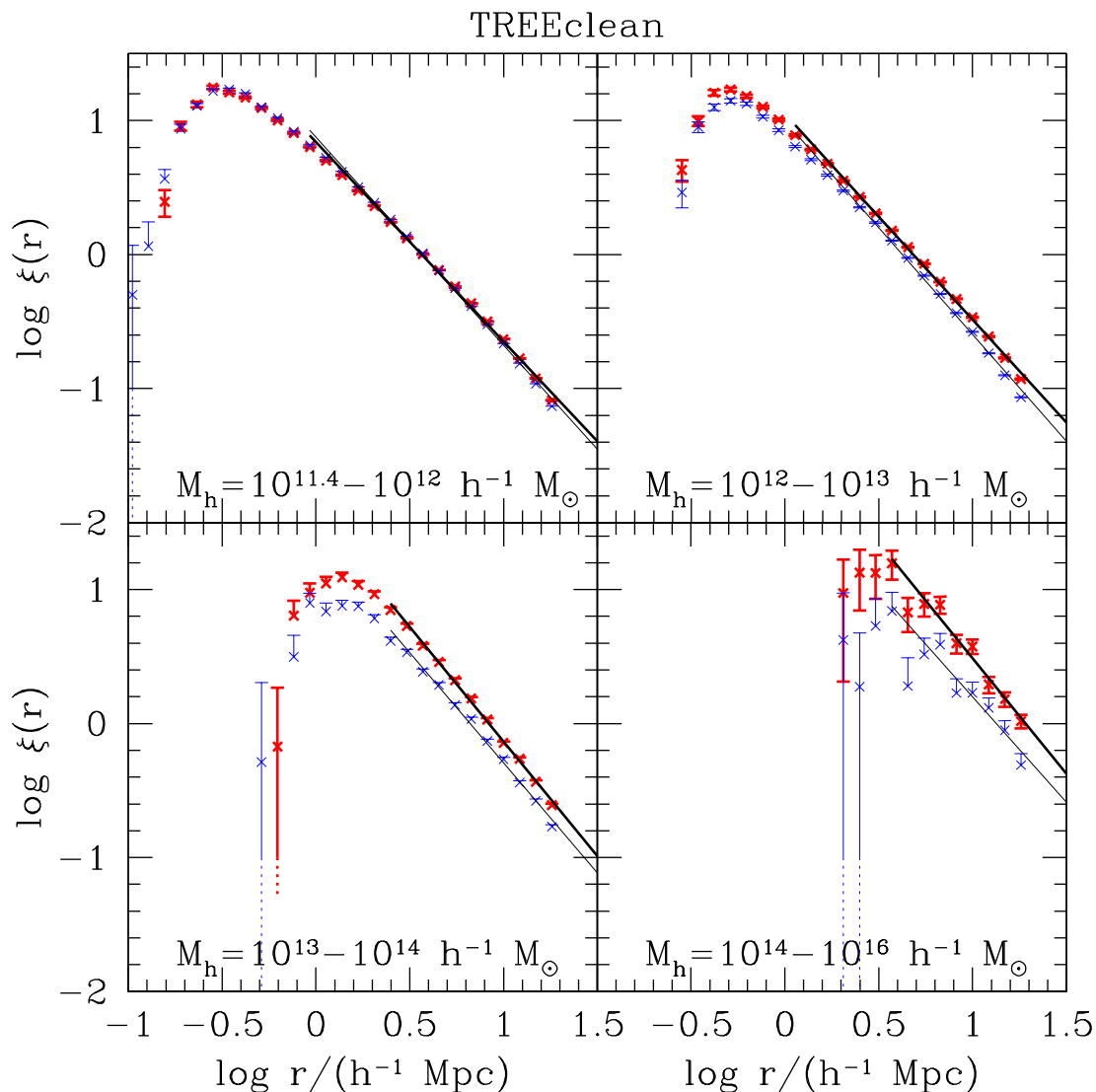


**Figure 18.** Two-point correlation function,  $\xi(r)$ , for TREEclean haloes in four mass bins. The lines represent power-law fits over the  $r$ -bins shown. The thick lines and red points are for haloes with  $\lambda \geq \lambda_{\text{med}}$  for that mass bin; the thin lines and blue points are for haloes with  $\lambda < \lambda_{\text{med}}$ . The data are noisy in the higher mass bins which contain fewer haloes. The error bars are Poisson errors, i.e. the square-root of the number of pairs in each  $r$ -bin, divided by the mean number of pairs per  $r$ -bin.

where  $\xi_{\text{hh}}(r|M_h, \lambda)$  denotes the halo-halo correlation function for haloes in a given range of mass and spin (in this example), and  $\xi_{\text{mm}}(r)$  is the dark matter correlation function. We compute the bias parameter as a function of mass,  $b(M_h)$ , using a similar method to that of Gao et al. (2005). Specifically, we compute  $\xi_{\text{hh}}(r|M_h, \lambda)$  in four  $r$ -bins in the

range  $6 \leq r \leq 25 h^{-1}\text{Mpc}$ , equally spaced in  $\log r$ . The bias parameter at each mass is then found as the normalisation constant that minimises:

$$\chi^2 = \sum_{i=1}^n \left( \frac{\xi_{\text{hh}}(r_i) - b^2 \xi_{\text{mm}}(r_i)}{\sigma_{\text{hh}}(r_i)} \right)^2 \quad (22)$$

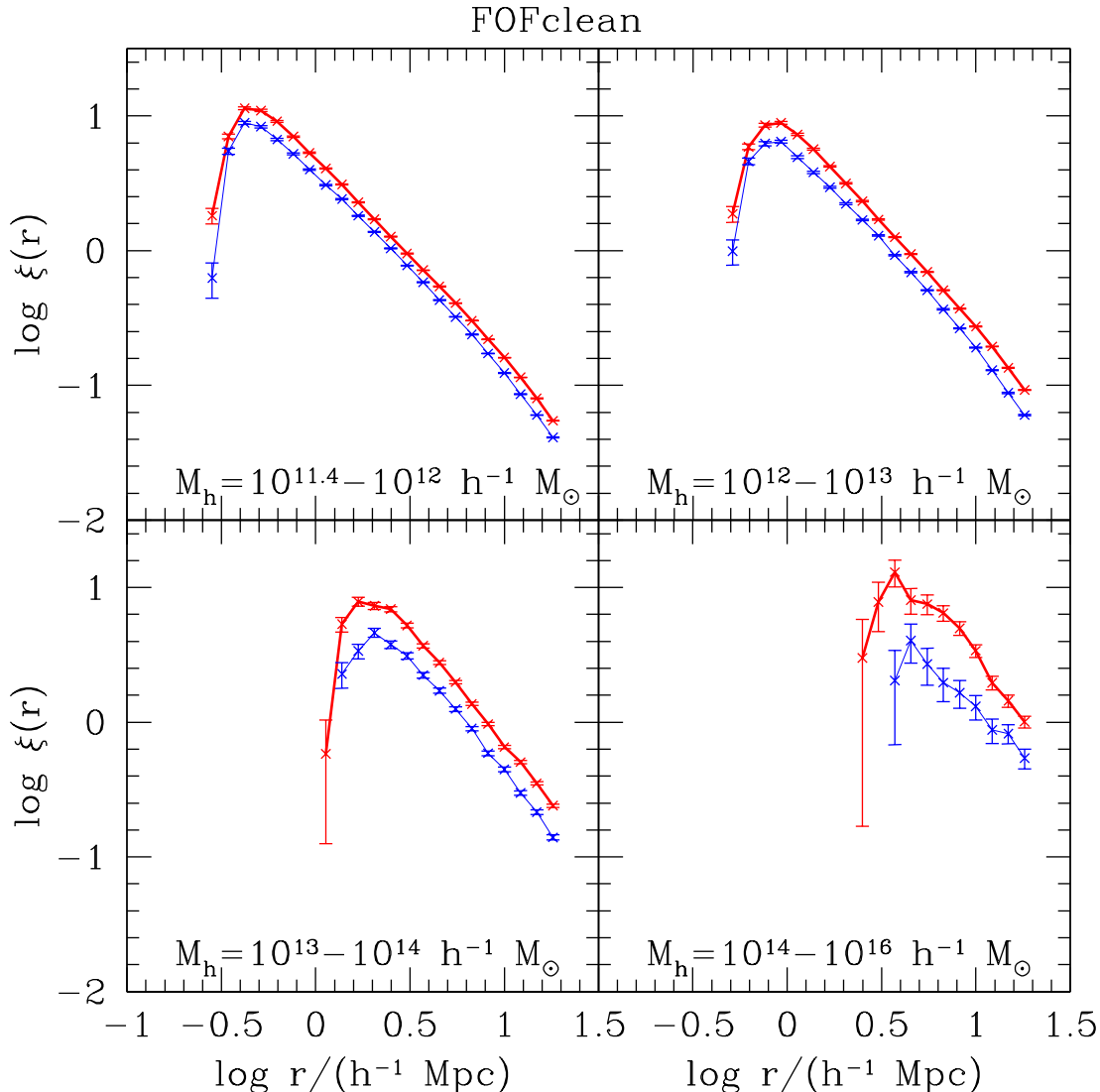


**Figure 19.** As Fig. 18, but for the FOFclean haloes. No fits were made to these data, and the lines merely join the points. For this catalogue, the higher spin haloes (thick red lines) are consistently and significantly more strongly clustered than the lower spin haloes (thin blue lines). The results for the SOclean haloes are very similar.

where the  $\sigma_{\text{hh}}(r_i)$  are the Poisson errors on  $\xi_{\text{hh}}(r_i)$ , and the sum is over all ( $> 1$ )  $r$ -bins where  $\xi_{\text{hh}}(r_i) > 0$  and  $\xi_{\text{hh}}(r_i)$  was computed using at least 100 objects. This procedure is performed first for all the TREEclean and FOFclean haloes. It is then repeated for the haloes in the upper and lower 20th percentiles of the  $\lambda$  and  $s$  distributions, from both catalogues.

The results are shown in Fig. 20. This shows that higher spin haloes are more clustered than the average, and the lower spin haloes are less clustered. This trend is largest at higher masses, reaching a factor of  $\approx 2.2$  between the high-spin and low-spin bias at the largest mass,  $\sim 2 \times 10^{14} h^{-1} M_{\odot}$ .

## 5 CONCLUSIONS

The huge size and high resolution of the Millennium simulation (Springel et al. 2005) makes it possible to determine the properties of dark matter haloes in the  $\Lambda$ CDM cosmology with unprecedented statistical power. In this paper, we have concentrated on the spins and shapes of dark matter haloes, ranging in mass from those of dwarf galaxies to those of rich clusters. We have investigated the distribution of the spin parameter,  $\lambda$ , its dependence on mass, the distribution of shapes, the relationship between shape and spin, and the environmental dependence of spin and shape. We provide accurate fitting formulae for several quantities of interest.

While many of the properties we have investigated here have been studied in earlier simulations going back over twenty years, a novel aspect of our work is the analysis and comparison of haloes identified in different ways. Alongside the traditional “friends-of-friends” (FOF) algorithm of

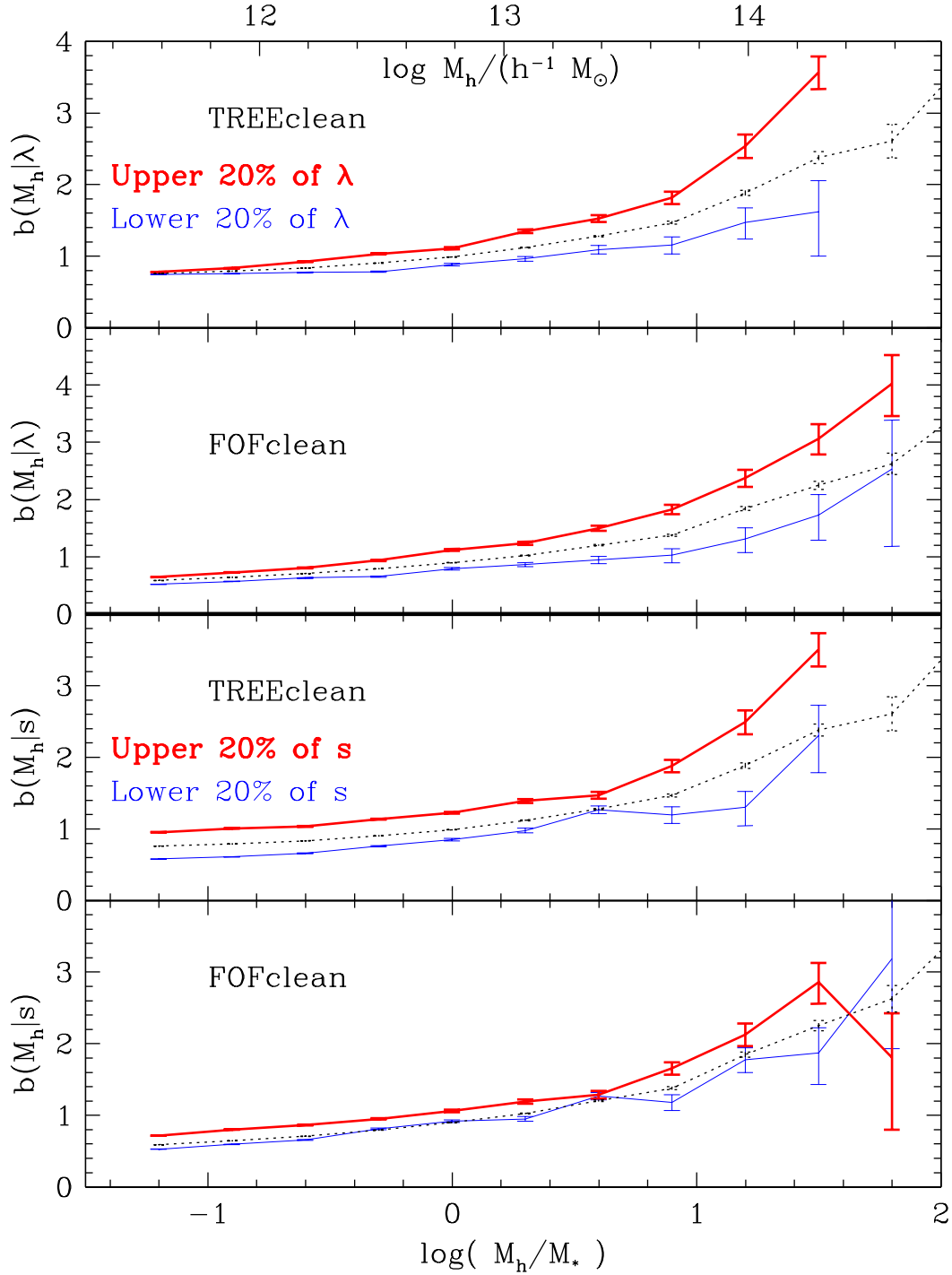


**Figure 20.** Bias parameter,  $b(M_h)$ , for the halo populations indicated in the legend. In each plot, the central dotted line marks the bias for the entire population at that mass. The thick red line is the bias for haloes in the upper 20 per cent of the distributions of  $\lambda$  (upper two plots) and  $s$  (lower two plots), and the thin blue line is for haloes in the lower 20 per cent of the distributions. The error bars give the  $\Delta\chi^2 = 1$  confidence interval. The lines stop either when the correlation function  $\xi(r)$  for at least 3 of the 4 radial bins is non-positive, or if it was made using fewer than 100 objects.

Davis et al. (1985) and the “spherical overdensity” (SO) algorithm of Lacey & Cole (1994), we have introduced a new halo definition, the TREE haloes, which are perhaps the most appropriate when carrying out comparisons of the simulation results with galaxy and cluster data. The TREE haloes are defined as branches of the halo merger trees, in which special care has been taken to identify physical haloes by separating objects that are artificially and transiently linked together. Each groupfinder results in more than 15 million haloes at  $z = 0$ .

The TREE halo catalogue was further ‘cleaned’ in two ways. Firstly, to remove any remaining spurious objects, we applied a cut in the instantaneous virial ratio, ( $-0.5 \leq \frac{2T}{U} + 1 \leq 0.5$ ). Secondly, to remove objects whose angular momentum is biased due to particle discreteness, we considered only haloes with more than 300 particles, as indicated by convergence tests. Our final cleaned halo catalogues consist of  $> 10^6$  haloes at  $z = 0$ .

We find that the distribution of the dimensionless spin parameter,  $P(\lambda)$ , is poorly fit by a lognormal when this many objects are considered. The function given by Eqn. 15 provides a much better description of the data. Although the distribution of  $\lambda(M_h)$  is fairly broad, there is a clear trend of the median spin with halo mass, with more massive haloes spinning more slowly. However, the strength and shape of the trend is significantly different for different halo definitions. The cubic polynomial of Eqn. 17 provides a very good fit to the median spin of the TREEclean halo catalogue, over a factor of  $\sim 10^3$  in halo mass.

We analysed the shapes of the haloes, and found, as in previous studies, that there is a broad distribution of shapes with a slight preference for prolateness over oblateness. More massive haloes are less spherical and more prolate in the median, although the data span a large fraction of the available shape parameter space. We fit broken lines to the trends with  $\log M_h$  of the median sphericity axis ratio  $s = c/a$  and the median triaxiality parameter  $\mathcal{T}$  (Eqn. 18). Both these quantities exhibit a change of behaviour at a galactic mass scale,  $M_h \approx 2 \times 10^{12} h^{-1} M_\odot$ , where the gradient of the fit changes sign, with haloes becoming increasingly aspherical and more prolate with increasing mass.

The rounder haloes have less coherent rotation, with a median spin that is independent of mass ( $\lambda_{\text{med}}(s \gtrsim 0.9) \approx 0.033$ ). The most massive haloes have a median spin that is independent of sphericity ( $\lambda_{\text{med}}(s) \approx 0.032$ ). However, there is significantly less correlation between the nature of halo triaxiality (prolateness *vs* oblateness) and the spin parameter. Although the haloes are far from being rotationally supported, there is a strong preference for the spin vector to be aligned parallel to the halo minor axis and to be perpendicular to the major axis. The tendency for the spin to be perpendicular to the intermediate axis is significantly weakened by the prevalence of prolate shapes for which there is a near degeneracy between the intermediate and minor axes.

We find a clear signal that the spins and shapes of haloes are sensitive to the cosmological environment: more rapidly rotating haloes of a given mass are more strongly clustered. The strength of this effect increases with halo mass. It is weak for subgalactic and galactic haloes, but can be larger than a factor of  $\sim 2$  for galaxy cluster haloes. A similar effect is seen when examining halo shapes: more spherical haloes are more strongly clustered, with a greater signal at

higher masses. Our result adds further evidence to the recent finding by Gao et al. (2005), also from analysis of the Millennium Run, that the internal properties of haloes depend not only upon their mass but also upon the environment in which they form.

The huge number of haloes in the  $\Lambda$ CDM Millennium simulation enables us to characterise the distribution of halo spins, and their relation to halo mass, shape and clustering, with unprecedented precision. However, we have also shown the significance of a careful halo definition. The properties of haloes defined and identified in different ways are noticeably different, and it is important to make the appropriate choice for a given application. For comparisons with real data, we recommend using the new class of “TREE” haloes which we have investigated in this work.

## ACKNOWLEDGEMENTS

PB acknowledges receipt of a PhD studentship from the Particle Physics and Astronomy Research Council. VRE is a Royal Society University Research Fellow. CSF is a Royal Society-Wolfson Research Merit Award holder. The simulation and analysis used in this paper was carried out as part of the programme of the Virgo Consortium on the Regatta supercomputer of the Computing Centre of the Max-Planck-Society in Garching, and the Cosmology Machine supercomputer at the Institute for Computational Cosmology, Durham.

## REFERENCES

- Allgood B., Flores R. A., Primack J. R., Kravtsov A. V., Wechsler R. H., Faltenbacher A., Bullock J. S., 2006, *MNRAS*, 367, 1781
- Avila-Reese V., Colín P., Gottlöber S., Firmani C., Mautsches C., 2005, *ApJ*, 634, 51
- Bailin J., Steinmetz M., 2005, *ApJ*, 627, 647
- Barnes J., Efstathiou G., 1987, *ApJ*, 319, 575
- Bower R. G., Benson A. J., Malbon R., Helly J. C., Frenk C. S., Baugh C. M., Cole S., Lacey C. G., 2006, *MNRAS*, 370, 645
- Bryan G. L., Norman M. L., 1998, *ApJ*, 495, 80
- Bullock J. S., 2002, in Natarajan P., ed., *Proceedings of the Yale Cosmology Workshop “The Shapes of Galaxies and Their Dark Matter Halos”*, New Haven, Connecticut, USA, 28-30 May 2001. Singapore: World Scientific, 2002, ISBN 9810248482. *Shapes of dark matter halos (astro-ph/0106380)*. p. 109
- Catelan P., Theuns T., 1996, *MNRAS*, 282, 436
- Cole S., Lacey C., 1996, *MNRAS*, 281, 716
- Cole S., Lacey C. G., Baugh C. M., Frenk C. S., 2000, *MNRAS*, 319, 168
- Davis M., Efstathiou G., Frenk C. S., White S. D. M., 1985, *ApJ*, 292, 371
- Doroshkevich A. G., 1970, *Astrophysics*, 6, 320
- Efstathiou G., Jones B. J. T., 1979, *MNRAS*, 186, 133
- Eke V. R., Cole S., Frenk C. S., 1996, *MNRAS*, 282, 263
- Faltenbacher A., Gottlöber S., Kerscher M., Müller V., 2002, *A&A*, 395, 1
- Franx M., Illingworth G., de Zeeuw T., 1991, *ApJ*, 383, 112

- Frenk C. S., White S. D. M., Davis M., Efstathiou G., 1988, *ApJ*, 327, 507
- Gao L., Springel V., White S. D. M., 2005, *MNRAS*, 363, L66
- Gardner J. P., 2001, *ApJ*, 557, 616
- Gelb J. M., Bertschinger E., 1994, *ApJ*, 436, 467
- Gill S. P. D., Knebe A., Gibson B. K., 2004, *MNRAS*, 351, 399
- Gottlöber S., Turchaninov V., 2006, in *EAS Publications Series. Halo Shape and its Relation to Environment* (astro-ph/0511675). pp 25–28
- Governato F., Moore B., Cen R., Stadel J., Lake G., Quinn T., 1997, *New Astronomy*, 2, 91
- Harker G., Cole S., Helly J., Frenk C., Jenkins A., 2006, *MNRAS*, 367, 1039
- Helly J. C., Cole S., Frenk C. S., Baugh C. M., Benson A., Lacey C., 2003, *MNRAS*, 338, 903
- Hopkins P. F., Bahcall N. A., Bode P., 2005, *ApJ*, 618, 1
- Hoyle F., 1949, in *Burgers J. M., van de Hulst H. C., eds, Problems of Cosmical Aerodynamics, The origin of the rotations of the galaxies.* Central Air Documents Office, Dayton, OH, pp 195–197
- Kasun S. F., Evrard A. E., 2005, *ApJ*, 629, 781
- Klypin A., Gottlöber S., Kravtsov A. V., Khokhlov A. M., 1999, *ApJ*, 516, 530
- Lacey C., Cole S., 1994, *MNRAS*, 271, 676
- Lee J., Pen U.-L., 2000, *ApJ*, 532, L5
- Lemson G., et al., 2006, preprint (astro-ph/0608019)
- Lemson G., Kauffmann G., 1999, *MNRAS*, 302, 111
- Macciò A. V., Dutton A. A., van den Bosch F. C., Moore B., Potter D., Stadel J., 2006, preprint (astro-ph/0608157)
- Merritt D., Sellwood J. A., 1994, *ApJ*, 425, 551
- Mo H. J., Mao S., White S. D. M., 1998, *MNRAS*, 295, 319
- Padmanabhan T., 1993, *Structure formation in the Universe.* Cambridge Univ. Press, Cambridge
- Peebles P. J. E., 1969, *ApJ*, 155, 393
- Peebles P. J. E., 1971, *A&A*, 11, 377
- Percival W. J., et al., 2002, *MNRAS*, 337, 1068
- Porciani C., Dekel A., Hoffman Y., 2002, *MNRAS*, 332, 325
- Reed D., Governato F., Quinn T., Gardner J., Stadel J., Lake G., 2005, *MNRAS*, 359, 1537
- Sánchez A. G., Baugh C. M., Percival W. J., Peacock J. A., Padilla N. D., Cole S., Frenk C. S., Norberg P., 2006, *MNRAS*, 366, 189
- Shaw L. D., Weller J., Ostriker J. P., Bode P., 2006, *ApJ*, 646, 815
- Spergel D. N., et al., 2003, *ApJS*, 148, 175
- Spergel D. N., et al., 2006, preprint (astro-ph/0603449)
- Springel V., et al., 2005, *Nature*, 435, 629
- Springel V., White S. D. M., Tormen G., Kauffmann G., 2001, *MNRAS*, 328, 726
- Springel V., Yoshida N., White S. D. M., 2001, *New Astronomy*, 6, 79
- Tegmark M., et al., 2004, *Phys. Rev. D*, 69, 103501
- Tonini C., Lapi A., Shankar F., Salucci P., 2006, *ApJ*, 638, L13
- van den Bosch F. C., 1998, *ApJ*, 507, 601
- Vitvitska M., Klypin A. A., Kravtsov A. V., Wechsler R. H., Primack J. R., Bullock J. S., 2002, *ApJ*, 581, 799
- Warren M. S., Quinn P. J., Salmon J. K., Zurek W. H., 1992, *ApJ*, 399, 405
- Wechsler R. H., Zentner A. R., Bullock J. S., Kravtsov A. V., Allgood B., 2005, preprint (astro-ph/0512416)
- Weinberg D. H., Hernquist L., Katz N., 1997, *ApJ*, 477, 8
- Wetzel A. R., Cohn J. D., White M., Holz D. E., Warren M. S., 2006, preprint (astro-ph/0606699)
- White S. D. M., 1984, *ApJ*, 286, 38
- White S. D. M., Frenk C. S., 1991, *ApJ*, 379, 52
- White S. D. M., Rees M. J., 1978, *MNRAS*, 183, 341

## APPENDIX A: EXAMPLES OF HALOES

The following plots give examples of haloes from our catalogues, chosen as clear examples of various (usually undesirable) groupfinder effects – they are *not* ‘typical’ haloes from their respective catalogues. We show them to give some visual intuition as to the problems that can be encountered with different group-finding algorithms, as described in section 3.

The first three show FOF haloes with unusual properties in real and velocity space. Fig. A1 shows a halo that is clearly made up of at least two objects joined via tenuous bridge in. We show a more massive halo that nevertheless consists of many linked objects in Fig. A2. Fig. A3 shows a very distorted object located near a much larger halo.

The final two figures compare the results of the three different group-finding algorithms used. Figs A4 and A5 compare haloes defined using the FOF, SO and TREE algorithms. In both cases, projections of the selected FOF halo (and its neighbours) are shown in the left-hand panels, and the corresponding SO/TREE halo and neighbours are in the right-hand panels. The selected haloes (green) have, again, been chosen to provide a striking illustration of the effects of different algorithms. The more ‘normal’ haloes in the background (blue) are less strongly affected by the choice of groupfinder.

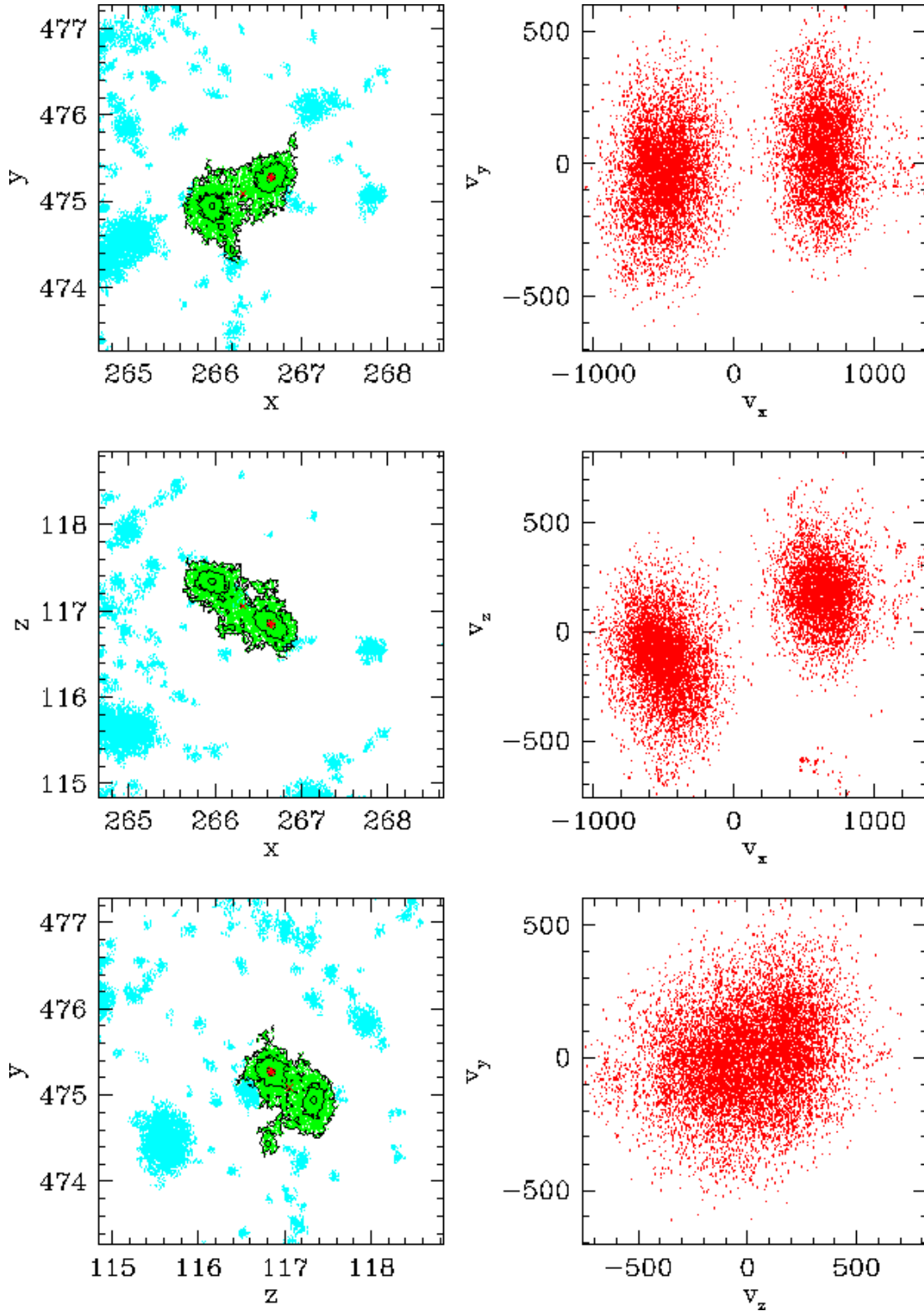


**Figure A1.** An example of a FOF halo made of two objects linked by a tenuous bridge. The left-hand panels show projections of the halo (overplotted in green) and its neighbours within  $2h^{-1}\text{Mpc}$  (blue) in real space, in units of  $h^{-1}\text{Mpc}$ . The black contours show projected particle density, at 1, 10 and 100 particles per contouring bin. The potential-minimum centre of the main halo is marked with a red star, and the centre-of-mass is marked with a red cross. The right-hand panels show the particles of the selected halo in velocity space, in  $\text{km s}^{-1}$ . This halo has a mass of  $M_h = 11418m_p \approx 9.82 \times 10^{12} h^{-1}M_\odot$ , and a spin parameter of  $\lambda = 1.5712$ . Its virial ratio,  $\frac{2T}{U} + 1 = -4.23$  means it is excluded from the FOFclean catalogue.

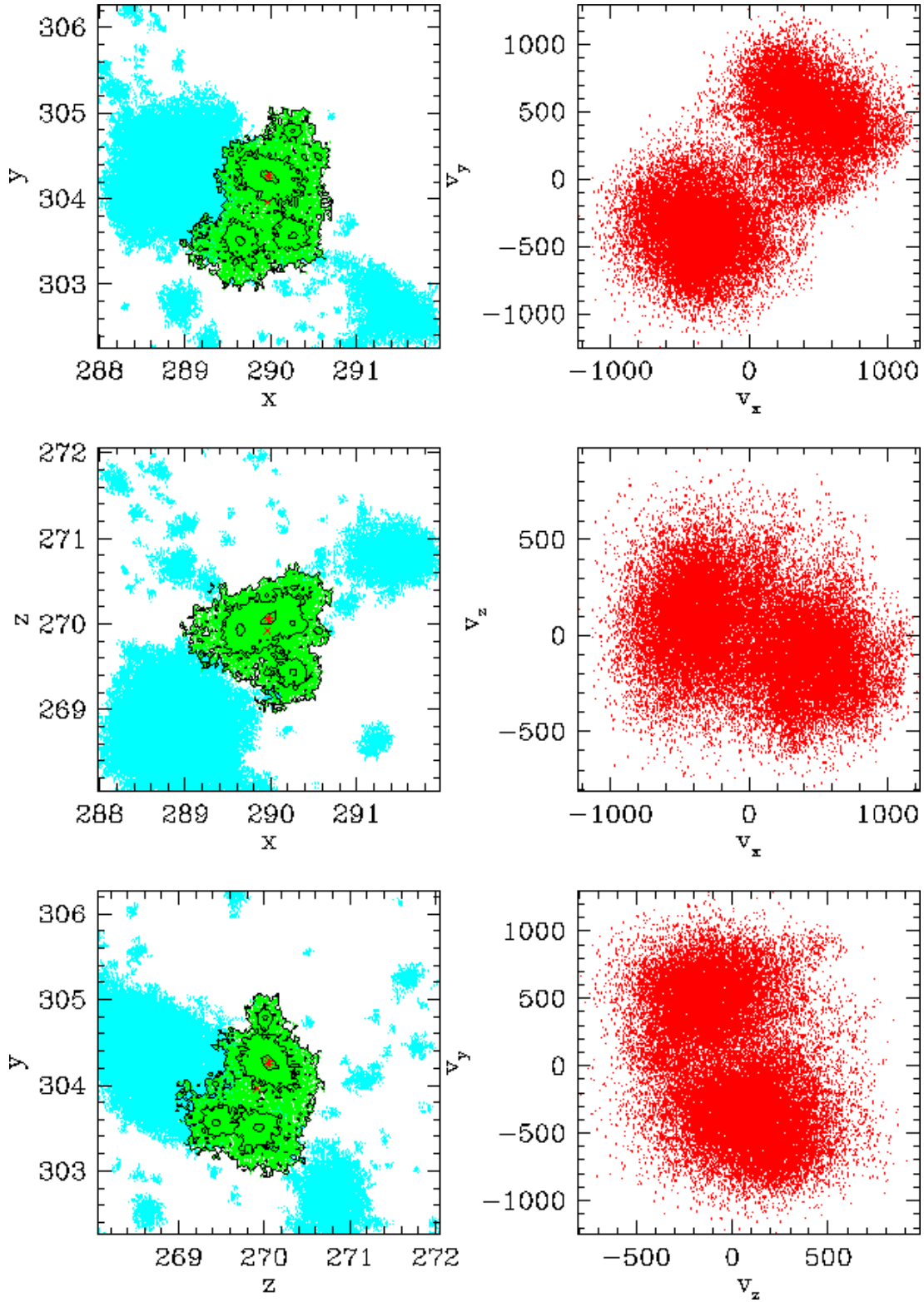


**Figure A2.** As Fig. A1, but showing an example of a larger multi-object FOF halo. This halo has a mass of  $M_h = 38741m_p \approx 3.33 \times 10^{13} h^{-1} M_\odot$ , and a spin parameter of  $\lambda = 0.3295$ . Its virial ratio,  $\frac{2T}{U} + 1 = -2.05$  means it is excluded from the FOFclean catalogue.

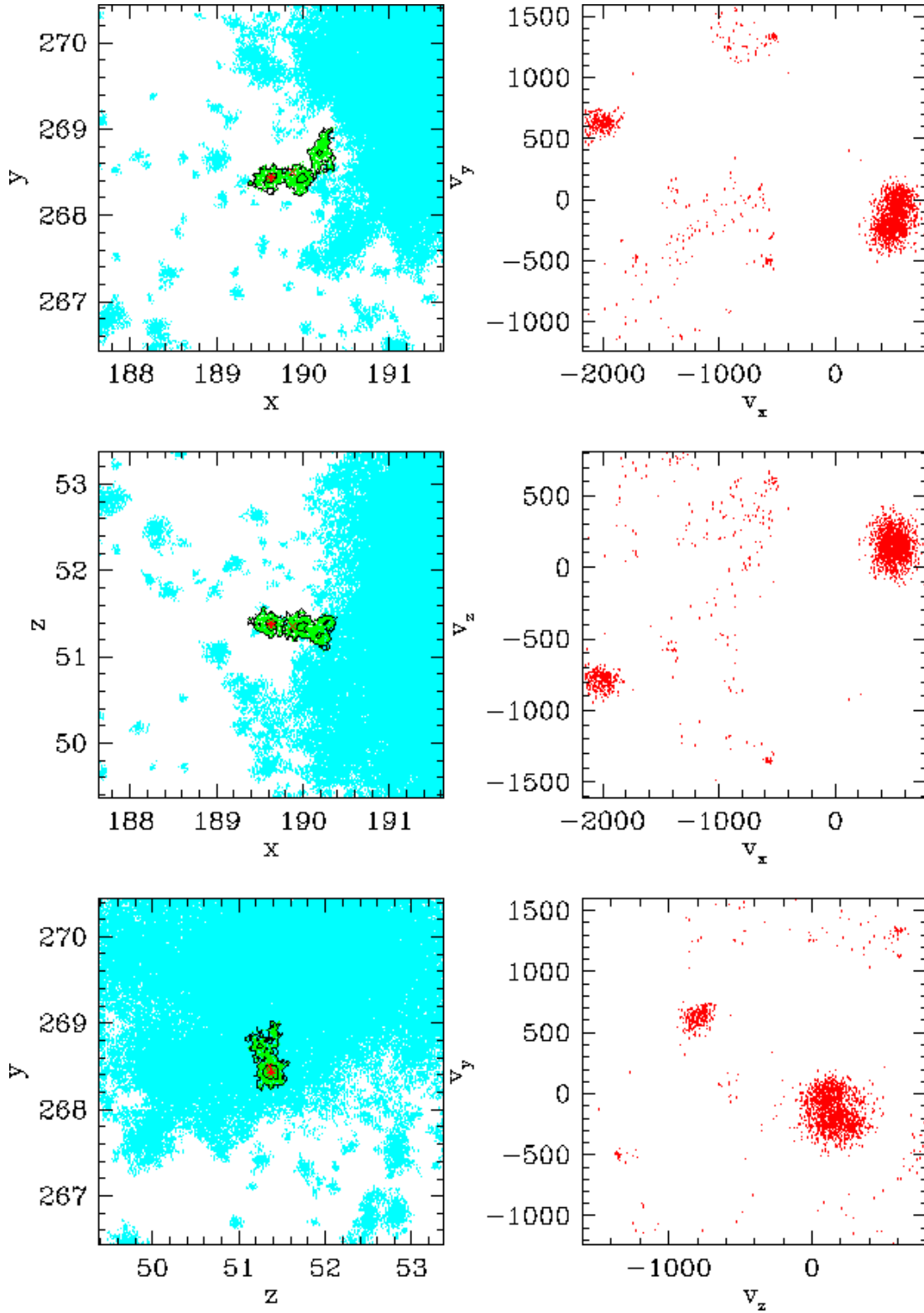


**Figure A3.** As Fig. A1, but showing an example of a small FOF halo with a large neighbour. The selected halo has a mass of  $M_h = 1967m_p \approx 1.69 \times 10^{12} h^{-1} M_\odot$ , and a spin parameter of  $\lambda = 17.60$ . Its virial ratio,  $\frac{2T}{U} + 1 = -53.8$  means it is excluded from the FOFclean catalogue.

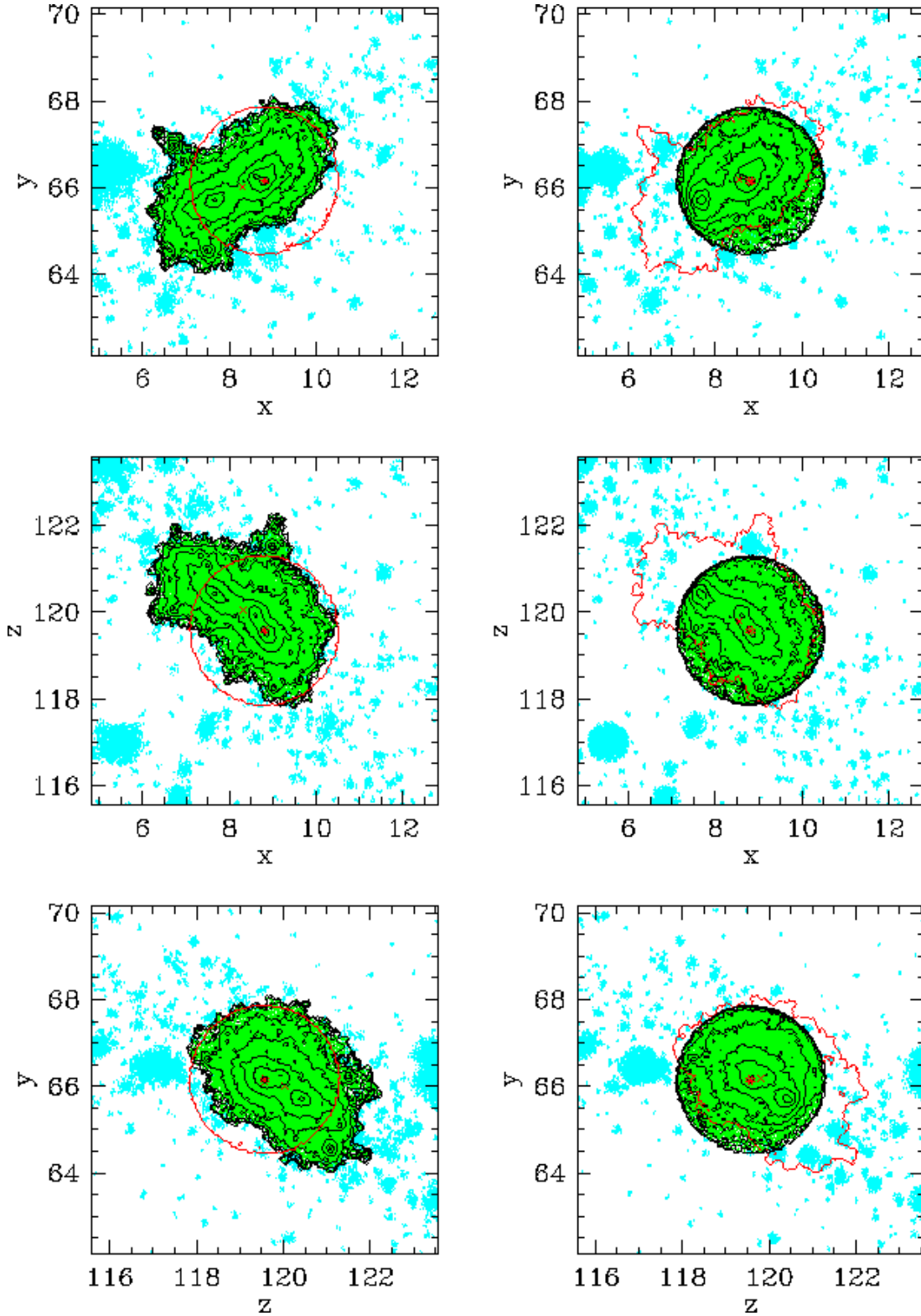


**Figure A4.** As Fig. A1, but showing a comparison of a massive FOF halo (left) and the corresponding SO halo (right), and their neighbours in each catalogue within  $4h^{-1}\text{Mpc}$ . A random sample of  $1/4$  of the particles are plotted; this doesn't effect the overall image of the halo. Projected logarithmic density-contours are plotted in black, spaced every factor of  $\sqrt{10}$  between 1 and  $10^{3.5}$  particles per contouring bin. The outermost contour (the halo boundary) is reproduced on the opposite panel in red. Note how the SO halo includes particles that were not part of the FOF group, and are much less dense than the halo proper. The FOF halo has a mass of  $M_h = 744\,019m_p \approx 6.40 \times 10^{14} h^{-1}M_\odot$ , and a spin of  $\lambda = 0.05959$ . It has a virial ratio of  $\frac{2T}{U} + 1 = -0.262$ , so it is included in the FOFclean catalogue. The SO halo has a mass of  $M_h = 610\,023m_p \approx 5.25 \times 10^{14} h^{-1}M_\odot$ , and a spin of  $\lambda = 0.04539$ . It has a virial ratio of  $\frac{2T}{U} + 1 = -0.332$ , slightly less relaxed than its FOF counterpart but still included in the SOclean catalogue.

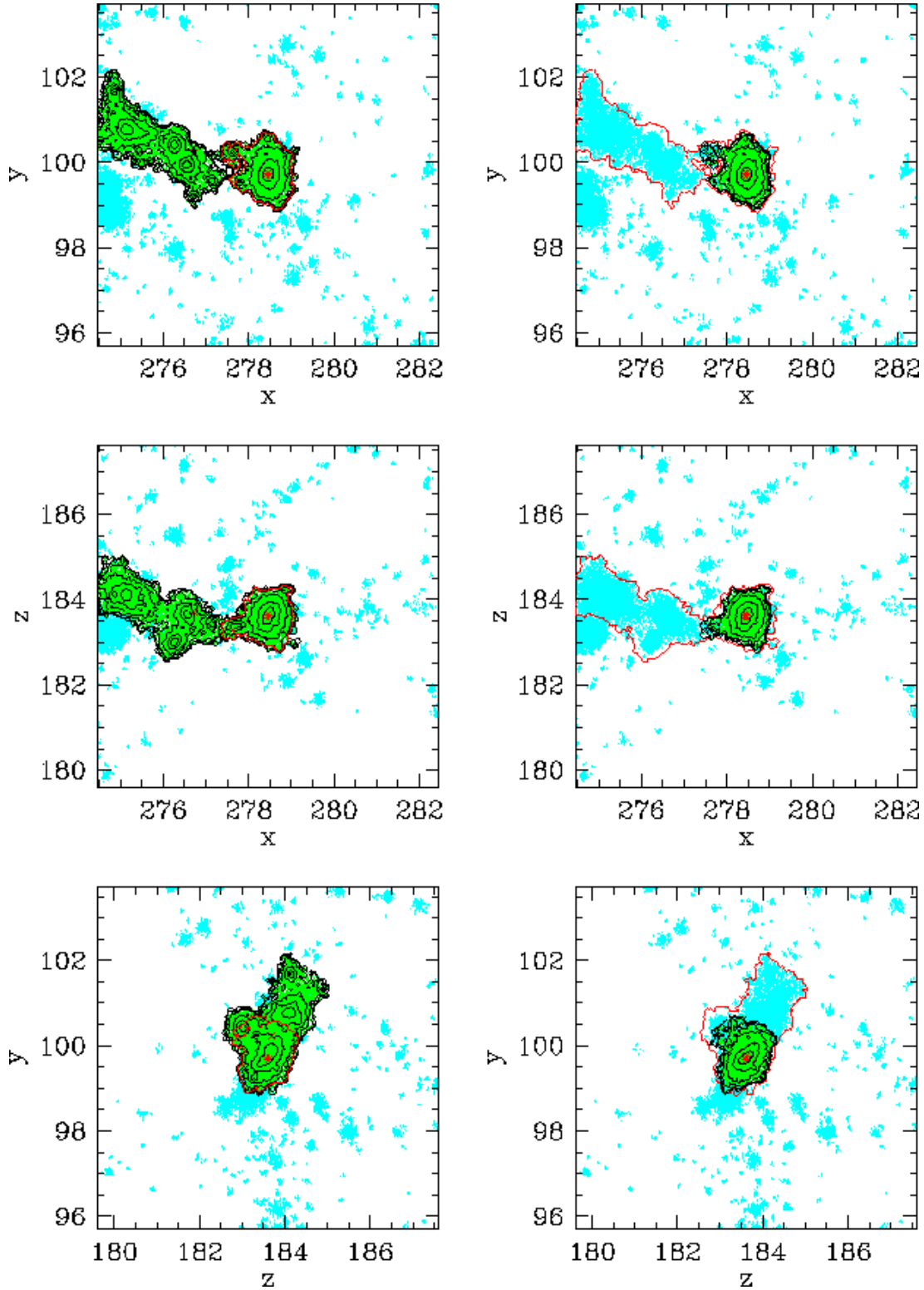


**Figure A5.** As Fig. A4, but comparing a massive FOF halo (left) and the corresponding TREE haloes (right). Again, a random selection of 1/4 of the points are plotted, and the density contours are spaced every factor of  $\sqrt{10}$  up to  $10^{2.5}$  particles per contouring bin. Note how the FOF halo is highly extended, with the subhalo housing the potential minimum being linked to a large neighbouring halo. The TREE catalogue splits these into two objects. The FOF halo has a mass of  $M_h = 126\,033m_p \approx 1.08 \times 10^{14} h^{-1}M_\odot$ , and a spin of  $\lambda = 0.1953$ . It has a virial ratio of  $\frac{2T}{U} + 1 = -0.111$ , so it is included in the FOFclean catalogue (despite its peculiar structure). The TREE halo has a much lower mass of  $M_h = 40\,719m_p \approx 3.50 \times 10^{13} h^{-1}M_\odot$ , and a spin of  $\lambda = 0.05711$ . It is slightly less relaxed however, with a virial ratio of  $\frac{2T}{U} + 1 = -0.159$ ; it is included in the TREEclean catalogue.